frontiers | Frontiers in Earth Science

TYPE Original Research
PUBLISHED 03 December 2024
DOI 10.3389/feart.2024.1501694

OPEN ACCESS

EDITED BY
Paterno Castillo,
University of California, San Diego,
United States

REVIEWED BY
Ian Ernest Masterman Smith,
The University of Auckland, New Zealand
May Sas,
Western Washington University, United States

*CORRESPONDENCE
L. Beloša,
lea.belosa@geo.uio.no,
belosa.lea@gmail.com

RECEIVED 25 September 2024
ACCEPTED 15 November 2024
PUBLISHED 03 December 2024

CITATION
Beloša L, Murphy DT, Ubide T, Callegaro S, Meyzen CM, Bizimis M and Mazzini A (2024) Magmatic evolution and architecture of an oceanic intraplate volcano: Vesteris Seamount, Atlantic Ocean.
Front. Earth Sci. 12:1501694.
doi: 10.3389/feart.2024.1501694

Magmatic evolution and architecture of an oceanic intraplate volcano: Vesteris Seamount, Atlantic Ocean

L. Beloša[1]*, D. T. Murphy[2], T. Ubide[3], S. Callegaro[1], C. M. Meyzen[4], M. Bizimis[5] and A. Mazzini[6,7]

[1]Centre for Planetary Habitability—PHAB, University of Oslo, Oslo, Norway, [2]School of Earth and Atmospheric Sciences, Queensland University of Technology, Brisbane, QLD, Australia, [3]School of the Environment, The University of Queensland, Brisbane, QLD, Australia, [4]Department of Geosciences, University of Padova, Padova, Italy, [5]Earth Ocean and Environment, College of Arts and Sciences, Columbia, SC, United States, [6]Department of Geosciences, University of Oslo, Oslo, Norway, [7]Reservoir Technology, Institute for Energy Technology (IFE), Kjeller, Norway

Vesteris is a large (33 × 27 km) and young (summit age: 0.65–0.010 Ma) intraplate seamount in the Greenland Sea, formed from ocean island basalt (OIB) magmatism. The volcano is composed of alkali basalt, basanite/tephrite, phonotephrite, mugearite, and benmoreite. Its phenocryst assemblage includes clinopyroxene, plagioclase, olivine, amphibole, rare haüyne, and oxides (Ti–magnetite and Cr–spinel), with phenocrysts hosting inclusions of apatite, sulfides (pyrrhotite), and melt. Despite its geological significance, the processes governing magma storage, ascent, and eruption dynamics remain poorly understood. To address this, we conducted detailed micro–chemical analyses of phenocrysts, groundmass microcrysts, melt inclusions, and groundmass glass. Using mineral–melt thermobarometry, we characterized the pre– to syn–eruptive crystallization conditions and reconstructed the architecture of the volcanic plumbing system. Our findings indicate that basanite liquids were primarily stored in the upper mantle (~6.4 kbar; ~22 km depth) with evidence of multi-level storage extending to ~9 kbar (~30 km depth). Textural and compositional zoning in clinopyroxenes suggests rapid magma ascent, while mafic recharge emerged as a key mechanism for remobilizing evolved clinopyroxene mush. Mafic recharge magmas also introduced early olivine crystals, which were later overgrown by high-Mg clinopyroxene upon mixing with more evolved melts. These results demonstrate that major crystal fractionation occurs in the upper mantle beneath Vesteris, resembling processes observed in low-flux ocean island basalt volcanoes. The evidence for rapid magma ascent highlights the dynamic nature of magma movement within the plumbing system, driven by mafic recharge and crystal-melt interactions.

KEYWORDS

intraplate volcanism, clinopyroxene zonation, thermobarometry, Vesteris Seamount, NE atlantic, clinopyroxene geochemistry, plumbing system architecture

1 Introduction

Seamounts constitute an integral phase of ocean island evolution and, contingent upon their dimensions and depths, stand as early manifestations in their complex

formation process (Staudingel and Clague, 2010). Volcanic islands often host human settlements and attract tourist activity, underscoring the imperative of understanding the potential hazards of eruptive activity. Early ocean island basalt (OIB) systems, such as the seamounts, are abundant yet enigmatic geological features (Gaina et al., 2017), but can provide key information on deep–seated mantle sources, e.g., (Fan et al., 2017; González-García et al., 2022; Zanon, 2015) and evolution through intricate magma plumbing systems.

Vesteris Seamount is the largest seamount on the NE Atlantic oceanic crust where the lithosphere is anomalously thick (Zhang et al., 2020). Recent studies postulated that the seamount is located above a divergence of an Iceland plume branch that extends northward from the Jan Mayen Fracture Zone (JMFZ) to the location of Vesteris Seamount in the Greenland basin (Beloša et al., 2024; Celli et al., 2021). The evolution of Vesteris lavas has been explained by simple closed–system magma fractionation (Moreno et al., 2021). However, recent studies of magma plumbing architecture in alkaline intraplate volcanoes, especially those based on mineral textures and compositions, show evidence of complex pre–eruptive histories in long–lived oceanic and continental systems (Klügel et al., 2015; Ubide et al., 2015; Tapu et al., 2023). Mineral textures and compositions retain valuable information on the magmatic processes across vertically extensive plumbing systems. This makes it possible to link volcanic eruptions with dynamic networks of magma transfer and storage that feed volcanism. Complex zoning patterns in phenocrysts attest to intricate magma histories that may include recharge, mixing, differentiation, ascent, and degassing through magmatic pathways that feed volcanism on Earth (Ubide and Kamber, 2018).

Here, we present a comprehensive analysis of textural and compositional features of phenocrysts in the Vesteris lava assemblage to reconstruct a subsurface plumbing system and potential eruption–triggering mechanisms. We study lava samples dredged from the volcanic flanks, focusing on magma storage conditions and processes recorded in clinopyroxene. Our data provide insights into magma storage and dynamics, including fractionation, recharge, and mixing of distinct magma batches in upper mantle reservoirs prior to eruption, which have broader implications for understanding the formation and development of larger OIB volcanoes.

2 Geological setting

The northeastern Atlantic Ocean floor is studded with seamounts (Gaina et al., 2017). The origins and distribution of these seamounts are linked to factors including seafloor spreading patterns, the cyclical activity of the Iceland plume, and significant tectonic events that have shaped the region, as described by Gernigon et al. (2009) and Gómez Dacal et al. (2023). Most of the seamounts and volcanic plateaus found to the south and north of the Jan Mayen Fracture Zone are thought to be associated with either the formation of mid–ocean ridges or the activity of the Icelandic plume (O'Connor et al., 2000). An alternative explanation involves the presence of a separate Jan Mayen plume, as discussed by Rickers et al. (2013) and Mertz et al. (2004).

The Vesteris Seamount stands out as a particularly noteworthy feature among these formations. This seamount is situated in the Greenland Basin at coordinates 73° 30′ N and 9° 10′ W (Figure 1A). Vesteris is the largest seamount on the northeastern Atlantic oceanic crust, with an aerial extension of 33 × 27 km, a height of approximately 3 km, and 800 km^3 of eruptive volume (Moreno et al., 2021; Haase and Devey, 1994). The Vesteris is a volcanic edifice with northeast–southwest elongation, sub–parallel to Mohn's and Kolbeinsey's active mid–ocean ridges, leading to suggestions that these bathymetric features may be related (Grønlie and Talwani, 1978; Hempel et al., 1991).

Recent studies integrating geophysical observations with isotopic data imply that Vesteris has a deep enriched source that is possibly correlated with a branch of the Icelandic plume that diverges north of the JMFZ (Beloša et al., 2024; Zhang et al., 2020). Radioisotopic dating via $^{40}Ar/^{39}Ar$ indicated that the Vesteris Seamount is younger than the ~44 Ma crust where it resides (Mertz and Renne, 1995; Gaina et al., 2009; Voss et al., 2009). The episodic formation of the seamount included trachybasaltic and tephritic eruptions between 0.50 and 0.65 Ma, followed by mugearitic eruptions between 0.010 and 0.085 Ma (Mertz and Renne, 1995). These findings, along with new bathymetric data and morpho–structural analyses, led Moreno et al. (2021) to propose a three–stage evolution model for this seamount: 1. An early stage characterized by deep, regional extensional lithospheric stresses leading to widespread effusive volcanism; 2. An intermediate stage marked by frequent volcaniclastic eruptions, influenced by a local stress field within the edifice; 3. The latest stage is characterized by flank collapses and the dislocation of cross–cutting ridges, followed by hyaloclastite deposition at the summit.

3 Methods

3.1 Sampling and sample preparation

Samples from the Vesteris Seamount were obtained during an East Greenland sampling (EGS; 2012) research campaign onboard RV Sermilik II. The samples were collected by lowering the dredge to ~900 m ocean depth and dredging along two opposite–facing slopes, SE (EGS12 – 94D) and NW (EGS12 – 93D), to 165 m and 186 m, respectively (Figure 1B). Beloša et al. (2024) provides a more detailed description of sample selection; the exact location of sampling in the volcanic edifice cannot be reconstructed, only the trajectory of the transect where the dredge passed. Hence, no immediate correlation between samples and volcanic stratigraphy can be deduced, as done instead by previous workers who have sampling location and age measurements for each sample, e.g., (Mertz and Renne, 1995; Moreno et al., 2021; Haase and Devey, 1994). Rock slabs with <1 cm thickness were cut out from each sample and prepared for bulk major (n = 12) and trace element analysis (n = 16) and radiogenic Sr–Nd–Pb–Hf isotope analysis (n = 12), as described in Beloša et al. (2024). For the present study, we prepared polished thin sections (n = 27) and resin mounts (n = 8) (Supplementary Figure S1) at the Institute for Energy Technology (IFE), Oslo, Norway. Final polishing was undertaken at the Geological Department of the University of Oslo, Norway. The thin sections were scanned at the Central Analytical Research Facility

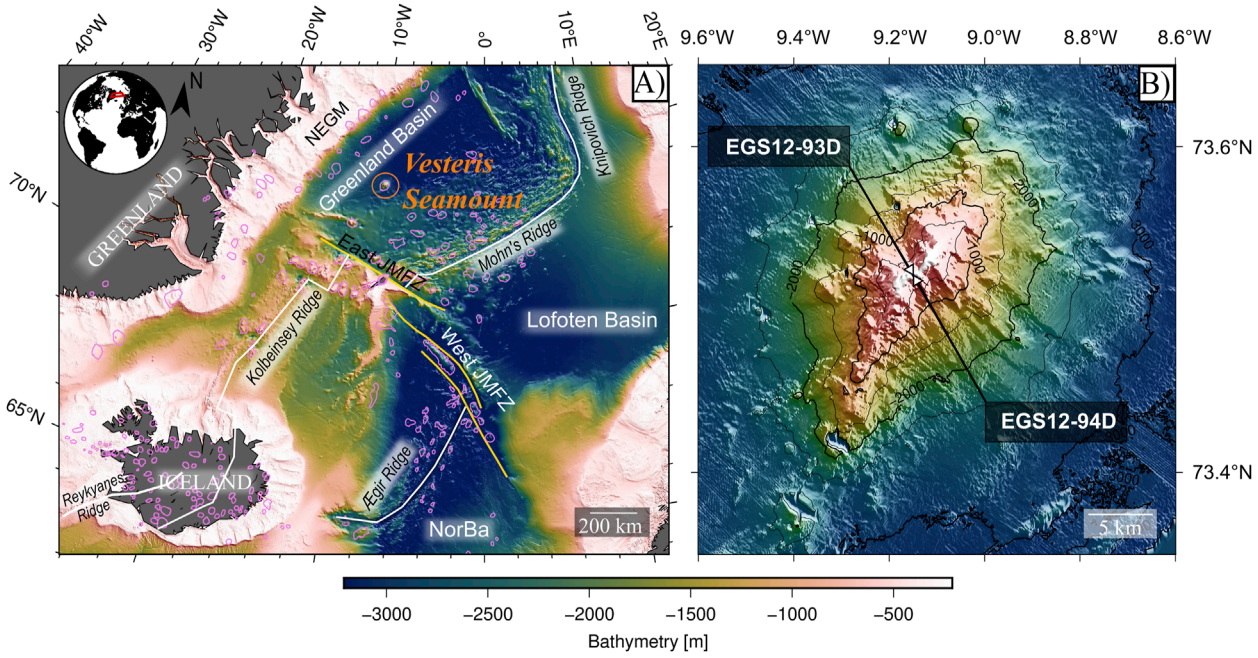

FIGURE 1
Bathymetrical map of **(A)** North–East Atlantic regional setting (GEBCO, 2021), **(B)** Vesteris Seamount bathymetry (MSM86 cruise; (Moreno et al., 2021)] with denoted dredged transects (black arrows): EGS 12 – 93D (SOL – 73.537701 N; 9.183944 W, EOL – 73.520879 N; 9.149131 W) and EGS 12 – 94D (SOL – 73.502981 N; 9.113111 W, EOL – 73.521535 N; 9.149729 W), modified from (Beloša et al., 2024). Mid–ocean ridge segments are represented with white lines and fracture zones as yellow lines (Müller et al., 2016). Pink polygons indicate the location of volcanic edifices (Gaina et al., 2017). Abbreviations: JMFZ, Jan Mayen Fracture Zone; NEGM, North East Greenland Margin; NorBa, Norwegian basin.

(CARF) at Queensland University of Technology (QUT), Brisbane, Australia. Using an Olympus VS200 Research Slide Scanner, we generated high optical resolution imagery of entire slides at high resolution, following the procedure of Acevedo Zamora and Kamber (2023). A link for digitalized scanned slides is in Supplementary Figure S1.

3.2 Mineral textural and chemical analysis

Samples were examined using an optical microscope and Hitachi SU5000 scanning electron microscope (SEM) at the Department of Geosciences at the University of Oslo. Scanning EM backscatter electron images (BSE) were used to image the crystals and select phases for quantitative electron microprobe analysis using a CAMECA SX100. At the Department of Geosciences at the University of Oslo. Mineral chemical analyses (n = 1638) were performed either along core–to–rim transects or as spots. In addition, we analyzed major elements in 52 groundmass glasses (basanites: n = 21; phonotephrites: n = 19; benmoreites: n = 12) and 62 glassy melt inclusions (24 olivine–hosted, 38 clinopyroxene–hosted). The total number of analyzed points in mineral phases varies from 513 in clinopyroxene (59 matrix crystals and 55 phenocrysts), 281 in plagioclase, 246 in olivine, 193 in amphibole, 115 in Fe–Ti oxides, 38 in haüyne, 33 in apatite, and 14 in sulfides (Supplementary Tables S1–S9).

We run EPMA wavelength dispersive spectroscopy (WDS) analysis with 15 kV accelerating voltage and 15 nA beam current for analyses performed on most mineral phases (olivine, clinopyroxene, amphibole, plagioclase, and sulfides) with a focused electron beam (0.1 μm, with an actual interaction area of ca. 2 × 2 μmm). Haüyne phenocrysts were analyzed using a 10 nA beam current with a defocused beam of 10 μm. For melt inclusions and groundmass glasses, a 2–5 μm beam and 10 μm beam were used, depending on the size of the target area. For apatite analysis, two–beam conditions were used to minimize the F and Cl migration, which may lead to excessively high F and Cl values (Stormer et al., 1993). Sodium, F, and Cl were analyzed first at a lower voltage of 10 kV and low beam current of 10 n, with the beam size of 5 μm for both (we measured F using the multilayered synthetic diffracting crystal PC1), and then P, Ca, S, Fe, Si were measured at 15 kV and 15 nA with the beam size of 5 μm. Matrix corrections were performed with the PAP procedure implemented in the CAMECA software (Pouchou and Pichoir, 1991). Calibration standards were as follows: wollastonite (Si, Ca), orthoclase (K), albite (Na), synthetic Al_2O_3 (Al), pure iron metal (Fe), pyrophanite (Mn, Ti), synthetic periclase (Mg), synthetic eskolaite Cr_2O_3 (Cr), nickel oxide (Ni), synthetic alforsite (Cl), fluorite (F), and Durango apatite (Ca, P, F for apatite analysis), synthetic Ce orthophosphate ($CePO_4$; (Jarosewich and Boatner, 1991) – P in glass), baryte (S in glass, apatite, and haüyne), and sphalerite (S in sulfide). We used stoichiometry and analytical totals to control the quality of pyroxene chemical data. For glass data, we monitored accuracy and precision using repeated measurements on the BCR 2G secondary standard (Supplementary Table S10; http://georem.mpch–mainz.gwdg.de/) with our runs. Accuracy for measured oxides was typically better than 5%, except for MnO

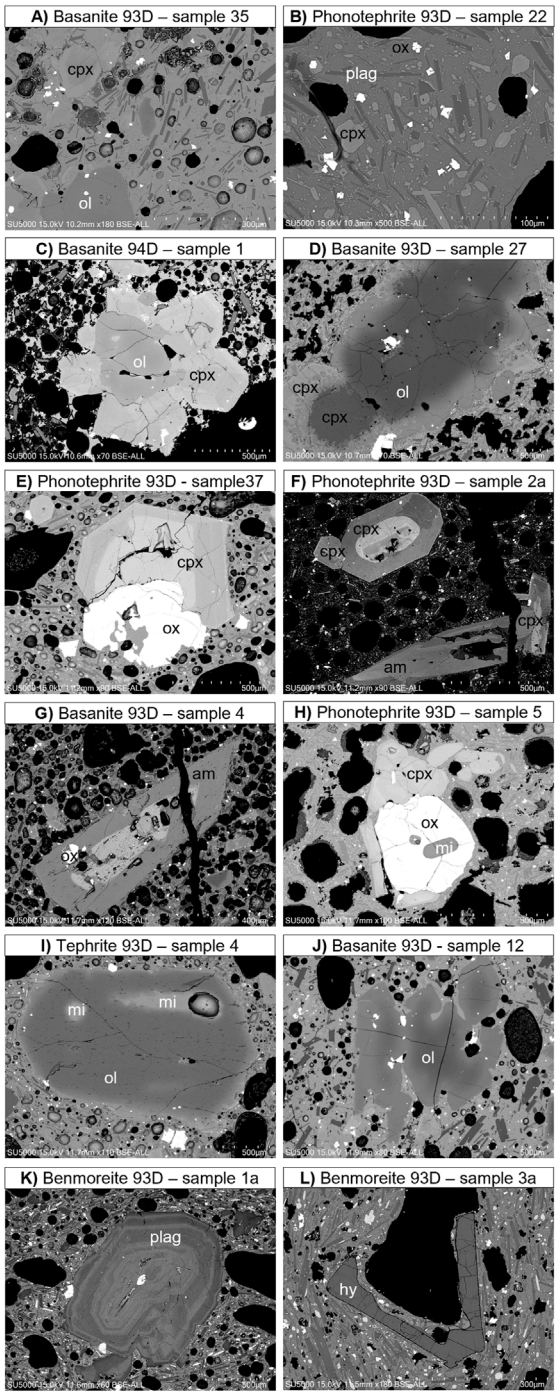

FIGURE 2
Representative back–scattered electron (BSE) images showing textural features of different lithotypes from Vesteris Seamount: Groundmass of **(A)** basanite and **(B)** phonotephrite with abundant oriented microlithic plagioclase laths, clinopyroxenes and oxides set in glassy matrix; **(C)** glomerocryst including anhedral olivine overgrown radially by clinopyroxene with oxide inclusions; **(D)** antecrystic anhedral olivine overgrown by clinopyroxene; **(E)** glomerocryst of anhedral oxide and euhedral reversely zoned clinopyroxene with a low-Mg core (bright BSE, dark green in plane polarized light (PPL)) and a high-Mg (darker BSE mantle, light green in PPL) that is sector–zoned; **(F)** top – euhedral sector zoned clinopyroxene overgrowing a low-Mg resorbed core, bottom – euhedral amphibole with a resorbed core; **(G)** reversely zoned euhedral amphibole with partially resorbed core with empty internal cavities, melt inclusions and oxides; **(H)** glomerocryst of subhedral oxide with melt inclusion and patchy zoned subhedral clinopyroxene; **(I)** subrounded olivine with diffusion rim, melt embayment and embedded oxides; **(J)** skeletal olivine with diffusion rim; **(K)** oscillatory zoned zoned plagioclase; **(L)** skeletal ha$ü$yne phenocryst. Abb: am, amphibole; cpx, clinopyroxene; hy, ha$ü$yne; mi, melt inclusion; ox, oxides; ol, olivine; plag, plagioclase.

(10%). Precision was 0.5%–1.7%, calculated as relative standard deviation (RSD), except for MnO (18%).

4 Results

4.1 Petrography

Lavas from Vesteris Seamount consists of variably evolved alkaline mafic and intermediate rocks. These are classified as alkali basalt, basanite/tephrite, phonotephrite, mugearite, and benmoreite (total alkali–silica (TAS) classification (LeMaitre, 2002; Beloša et al., 2024); and show systematic differences in mineral assemblage under the microscope (Figure 2; Supplementary Figures S1, S2). All samples are porphyritic with phenocryst volume fractions ranging from 5 vol% to 40 vol% (see Supplementary Table S1), on a vesicle–free basis, except of an aphyric mugearite with no phenocrysts (sample 9a). Visual estimates of phenocryst volume fractions in the thin/thick sections are summarised in Supplementary Table S1. The vesicularity of samples ranges from 10 vol% to 60 vol%. Below, we describe the petrography of the samples within each of the three lithotypes identified at Vesteris.

4.1.1 Basanites/tephrites and alkali basalts

Basanites/tephrites are the most primitive samples (i.e., 14 basanites/tephrites with >or <10 vol% of normative Ol, respectively; (Le Maitre et al., 1989), and one alkali basalt) and are characterized by a crystalline groundmass. The samples show seriate to porphyritic textures with inequigranular phenocrysts (150 μm – 1 mm; Figure 2A). The alkali basalt (sample 15) has a holocrystalline texture with serpentinized olivine (Ol) and elongated oxides filling the space around phenocrysts (Supplementary Figure 3G1). The groundmass of basanites and tephrites consists of fine–grained (up to 150 μm), euhedral, elongated, microcrystalline trachytoid plagioclase (Figure 2A), amphibole, clinopyroxene, and skeletal, dendritic, oxide microlites surrounded by variable amounts of quenched glass. Both basanites and tephrites are highly vesicular (Figure 2). Tephrites are olivine–poor and amphibole–rich, but have clinoyroxene phenocryst fractions that are comparable to the ones in basanites (Supplementary Table S1). For simplicity, we hereafter refer to primitive samples in the basanite–tephrite range as basanites: since these are dominant in our suite. Most basanites are characterized by an olivine–clinopyroxene mineralogical assemblage, representing up to 30 vol% of the modal proportions. In basanites, opaque oxide phenocrysts are less common (~2 vol%). Amphiboles are fine–grained, euhedral, concentrically zoned, and include broken phenocrysts with resorbed cores hosting melt inclusions and oxides. Zoned amphibole

phenocrysts have dark brown cores (lighter in BSE) and light brown rims (darker in BSE), without observed reaction rims (Figure 2G; Supplementary Figure 3C1).

4.1.2 Mugearites and phonotephrites

Phonotephrites and mugearites make up the intermediate sample suite. The groundmass of mugearites shows a holocrystalline, intergranular texture with plagioclase microlites surrounded by clinopyroxene and oxides. In mugearites, phenocrysts are rare, and one sample is aphyric. Other samples are moderately phyric with up to 5 vol% phenocrysts, including zoned clinopyroxene, amphibole, and oxides (Supplementary Table S1). Phonotephrites have a vesicular, porphyritic texture (5–20 vol%) with plagioclase, clinopyroxene, and amphibole phenocrysts, as well as oxide microcrysts, surrounded by a glassy groundmass (Supplementary Table S1). The phonotephrite groundmass has a trachytoid texture and consists of clinopyroxene, plagioclase, and dendritic oxide microcrysts (Figure 2B). The phenocryst assemblage consists of euhedral amphibole and clinopyroxene with subordinate plagioclase and oxides. Oxides, amphibole, and clinopyroxene often form glomerocrysts (Figure 2H). Melt inclusions and embayments are widespread in phenocrysts, either as rounded elongated blobs or infills of resorbed crystal cores formed due to local dissolution (Supplementary Figure 3G2). Some of these seem entrapped along surface irregularities in the phenocrysts (i.e., cracks).

4.1.3 Benmoreites

The most evolved rocks are benmoreites with a mineralogical assemblage composed of plagioclase, amphibole, clinopyroxene, and haüyne with occasional oxides (Ti–magnetite) (Supplementary Table S1). Benmoreites are the only rock type of the Vesteris sample suite that hosts plagioclase phenocrysts (Figure 2K; Supplementary Figure 3D). Plagioclase phenocrysts are set in a microcrystalline (<0.5 mm in size) groundmass consisting of clinopyroxene, flow–oriented plagioclase, and Ti–magnetite microcrysts.

4.2 Crystal cargo

Clinopyroxene in all samples forms euhedral–subhedral green to dark green crystals of variable sizes (up to 3 mm) comprising up to 10 vol% of the modal crystal content (Supplementary Table S1). Clinopyroxene phenocrysts often have dark green rounded, patchy, and corroded cores, hollow in the middle or filled with melt embayments (Figure 2F). The majority of clinopyroxes are strongly zoned, with various patterns (Supplementary Figure 3B). In benmoreites, clinopyroxene phenocrysts show normal zoning, while in phonotephrites and basanites, they are reverse–zoned. As shown in Figure 2F, Supplementary Figures 2B, 3B, reverse zoning can be recognized by the association of dark green cores (bright BSE cores) surrounded by light green mantles (dark mantles in BSE). Reverse–zoned mantles show oscillatory or sector zoning or a combination of the two. Mantles and rims are typically euhedral (Figure 2E).

Plagioclase is often restricted to the rock matrix in Vesteris lavas, where it occurs as tabular to elongated microlites. However, in benmoreites, plagioclase is the most abundant phenocryst phase (up to 10%). Plagioclase appears as euhedral to subhedral phenocrysts of variable sizes ranging from 500 μm to 1 mm (Figure 2K; Supplementary Figure S4). Most phenocrysts show oscillatory or complex zoning. The latter can include a combination of oscillatory and patchy zoning with an irregular distribution of darker and brighter zones in BSE, as shown in Supplementary Figure 3D1. Most textural complexities are hosted in phenocryst cores, which range in size from ~100 μm to ~300 μm in radius. Sieved phenocryst with hollow (Supplementary Figure S3D2) or filled cores occur sporadically (Supplementary Figure S3D3, D5). When filled, the replenishment is composed of oxides and/or melt inclusions (Supplementary Figure 3D3). The cores are surrounded by thick mantles, generally showing oscillatory zoning followed by a regular change from darker to lighter BSE zones (Supplementary Figure S3D4). Rims are thin and dark in BSE. Plagioclase microcrysts show normal zoning.

Olivine occurs as fine to medium–grained (100 μm to 3 mm) phenocrysts (Figures 2I, J). Some olivine have anhedral, subrounded morphology and form glomerocrysts (long axis: 0.5–2 mm) with clinopyroxene overgrowth (Figure 2C; Supplementary Figure S5). In these cases, clinopyroxene crystals radiate as pale–colored zones (lighter in BSE) around colorless olivines (darker in BSE) with thick diffusion zones over corroded rims (Figures 2C, D; Supplementary Figure S3A4). Olivine phenocrysts are often fractured and host melt inclusions, enclosed opaque oxides, Cr–spinel, and Ti–magnetite (Supplementary Figures S3A1, A2). Olivine phenocrysts are normally zoned and often have thin (~10 μm) diffusion rims, although they can have larger diffusion zones. Skeletal olivines are rare (Figure 2J). More often, olivine phenocrysts are polyhedral with subhedral to anhedral crystal faces (Figure 2I).

Amphibole is, together with clinopyroxene, a dominant phenocryst in phonotephrites. Amphibole phenocrysts are euhedral to subhedral brown and brown–green hexagonal or prismatic crystals (300 μm – 1 mm in longitudinal axis) (Figure 2F; Supplementary Figure S2C). Amphiboles are often zoned, but no reaction rims were observed. Amphiboles are sometimes associated with clinopyroxenes and oxides in glomerocrysts. Amphibole phenocrysts are frequently cracked (Figure 2G) and usually have hollow, resorbed cores – voids that are occasionally filled with melt or apatite and sulfide inclusions (Figure 2G). Only the smallest amphibole phenocrysts (>0.1 mm) lack resorbed cores.

Iron–titanium oxides make up 1 to 5 vol% of the studied rocks. Phenocrysts have euhedral to subhedral morphology, while groundmass microcrysts exhibit skeletal growth (Supplementary Figure S3F1, F5). Oxides often form glomerocrysts with plagioclase and amphibole crystals and are often found as inclusions within clinopyroxene and olivine phenocrysts (Supplementary Figure S3A, B).

Accessory mineral phases include apatite and sulfides, while haüyne is an additional accessory phase only within the most evolved rocks (benmoreites). **Apatite** is present in all rock types. Generally, apatite occurs as rounded or elongated inclusions (ca 50 μm) within phenocrysts (Supplementary Figure S3D5) and occasionally as euhedral microcrysts within the most evolved rocks (Supplementary Figure S3G5). **Sulfides** occur as elongated, acircular, or rounded inclusions within oxides, clinopyroxene, amphibole, and apatite, both in primitive and evolved rocks

(Supplementary Figure S3F2). Sulfides are present only within the phenocrysts when apatites occur. **Haüyne**, a tectosilicate from the sodalite group with a distinct blue color, was first reported in benmoreites from Vesteris Seamount in Beloša et al. (2024). It forms euhedral to subhedral phenocrysts of 200–500 μm. Phenocrysts are cracked and often contain melt inclusions (Supplementary Figure S3E). Skeletal euhedral microcrysts are abundant in benmoreites (Figure 2L; Supplementary Figure S3E).

Melt embayments and inclusions are randomly distributed in phenocrysts of olivine, clinopyroxene, amphibole, plagioclase, and oxides. Irregular melt embayments are frequently associated with crystal fractures, although they can also occur within phenocrysts. Regardless of the host mineral, they can be glassy, partially or fully crystallized (Supplementary Figure S3G3, G4). Rounded and elongated melt inclusions not associated with fractures are rare but occur in phenocrysts of all mineral phases.

4.3 Whole–rock, glass, and mineral chemistry

We analyzed groundmass glasses, phenocrysts (clinopyroxene, plagioclase, olivine, amphibole, oxides, haüyne, in order of abundance), and inclusions of melt and mineral (apatite, sulfides, and oxides) by electron microprobe (n = 1547). Whole–rock major and trace element compositions of Vesteris samples are presented in Beloša et al. (2024), while groundmass glass and melt inclusion measurements are reported in Supplementary Tables S2, S3. The compositions of all analyzed clinopyroxene, plagioclase, olivine, amphibole, oxides and accessory minerals are provided in Supplementary Tables S4–S9, in order of appearance.

4.3.1 Whole rock

Whole rock analyses from Vesteris Seamount from Beloša et al. (2024) and Moreno et al. (2021) are plotted in Figure 3. Samples in this study are generally unaltered, as indicated by their low Loss On Ignition (LOI) values [0.14–1.12 wt% (Beloša et al., 2024)]. Lavas (n = 12) belong to the sodic alkaline magma series (Na_2O – 2.0 > K_2O) and classify as alkali basalt, basanite/tephrite, phonotephrite, mugearite, and benmoreite (TAS classification (Beloša et al., 2024)).

The samples are variably evolved with MgO ranging from 1.5 to 10.5 wt%. As shown in Figure 3, decreasing MgO contents are associated with increasing SiO_2 (45.25–56.32 wt%), Na_2O (2.93–6.57 wt%) and Al_2O_3 (13.69–19.36 wt%) contents (Figure 3). The FeO_{TOT} (total iron as Fe^{3+}), CaO, and TiO_2 correlate positively with MgO up to 4 – 6 Wt.%. FeO_{TOT} also shows a slightly positive correlation at higher MgO (>6 wt%). However, TiO_2 and CaO (to a lesser extent) appear to show a slightly negative correlation after a kink at ~ 5 wt% MgO, as described in previous work at Vesteris Beloša et al. (2024) and Moreno et al. (2021). Basanites display an almost invariant SiO_2 content with decreasing MgO compared to phonotephrites, mugearites, and benmoreites.

4.3.2 Groundmass glass

The compositions of groundmass glasses were determined for most of the rock suites of Vesteris Seamount (basanites, phonotephrites, and mugearites). Groundmass glasses are more evolved than whole–rock compositions of the same sample but show less variability (Figure 3; Supplementary Table S2). Groundmass MgO contents range from 0.44–4.9 wt%. Only the mean values for basanites, phonotephrites, and benmoreites are shown for clarity in Figure 3. Groundmass glasses generally fall or slightly extend the trends defined by whole–rock analyses (Figure 3). A notable characteristic of groundmass glasses compared to whole–rock samples is the lack of kink at ~5 wt% MgO since their compositions are more evolved (<5 wt% MgO). In diagrams of Al_2O_3, FeO, Na_2O and CaO as a function of MgO (Figure 3), basanite groundmass glasses partially overlap with the whole–rock compositions of more evolved mugearite and phonotephrites. Phonotephrite groundmass glasses are compositionally close to benmoreite and mugearite whole–rock compositions.

4.3.3 Melt inclusions

We analyzed glassy melt inclusions and glassy to partially crystallized embayments hosted in clinopyroxene and olivine (Figure 3; Supplementary Table S3). Olivine–hosted inclusions were only analyzed in MgO–rich samples (i.e., basanites), whereas clinopyroxene–hosted melt inclusions were also measured in more evolved rocks (i.e., basanites, phonotephrites, and benmoreites). The MgO in olivine melt inclusions ranges from 1.3 to 6 wt%, and clusters around 2 wt%. Clinopyroxene inclusions span a wider range in MgO (0.2–7.3 wt%) and cluster at lower MgO 1.5 wt% (Figure 3). Olivine–hosted inclusions systematically overlap with the mean major element composition of basanite groundmass glasses. In contrast, clinopyroxene–hosted melt inclusions entirely or partially overlap with the mean compositions of phonotephrite and benmoreite glasses (Figure 3). The high MgO end of clinopyroxene–hosted melt inclusions also overlaps with the mean basanite groundmass glass composition. Clinopyroxene melt inclusions are Si–Al–rich relative to olivine melt inclusions, which are Fe–Ti–Ca–rich. Overall, as previously observed for groundmass glass compositions, melt inclusion compositions generally show the same trend as the whole–rock compositions in the major element variation diagrams but with higher TiO_2 and lower SiO_2 for a given MgO than the whole–rock compositions (Figure 3).

4.3.4 Clinopyroxene

Clinopyroxene compositions are classified as diopside–salite–ferrosalite ((Deer, 1978); Figure 4). Bivariate clinopyroxene plots of major element oxides against Mg# (Mg# = 100 x Mg/(Mg + Fe_{TOT}), concentrations expressed on a molar basis and Fe_{TOT} representing total iron as Fe^{2+}) are shown in Figure 4. The three rock types (i.e., basanite, mugearite, and phonotephrite) host clinopyroxene with broadly similar compositions (from 46 Mg# to 85 Mg#) and similar morphological features but show some compositional variations (Figure 4). From most evolved to least evolved (right to left column in Figure 4), the clinopyroxene shows a positive correlation between Mg# and SiO_2 and negative correlations between Mg# and Na_2O, Al_2O_3 and TiO_2.

As shown on Mg# variation diagrams, where the clinopyroxene compositions of basanites and phonotephrites (left and middle columns of Figure 4) are reported, a stand–alone clinopyroxene cluster is an outlier of the main correlation trend. Clusters with lower Mg# than the main trend (filled symbols) represent low-Mg

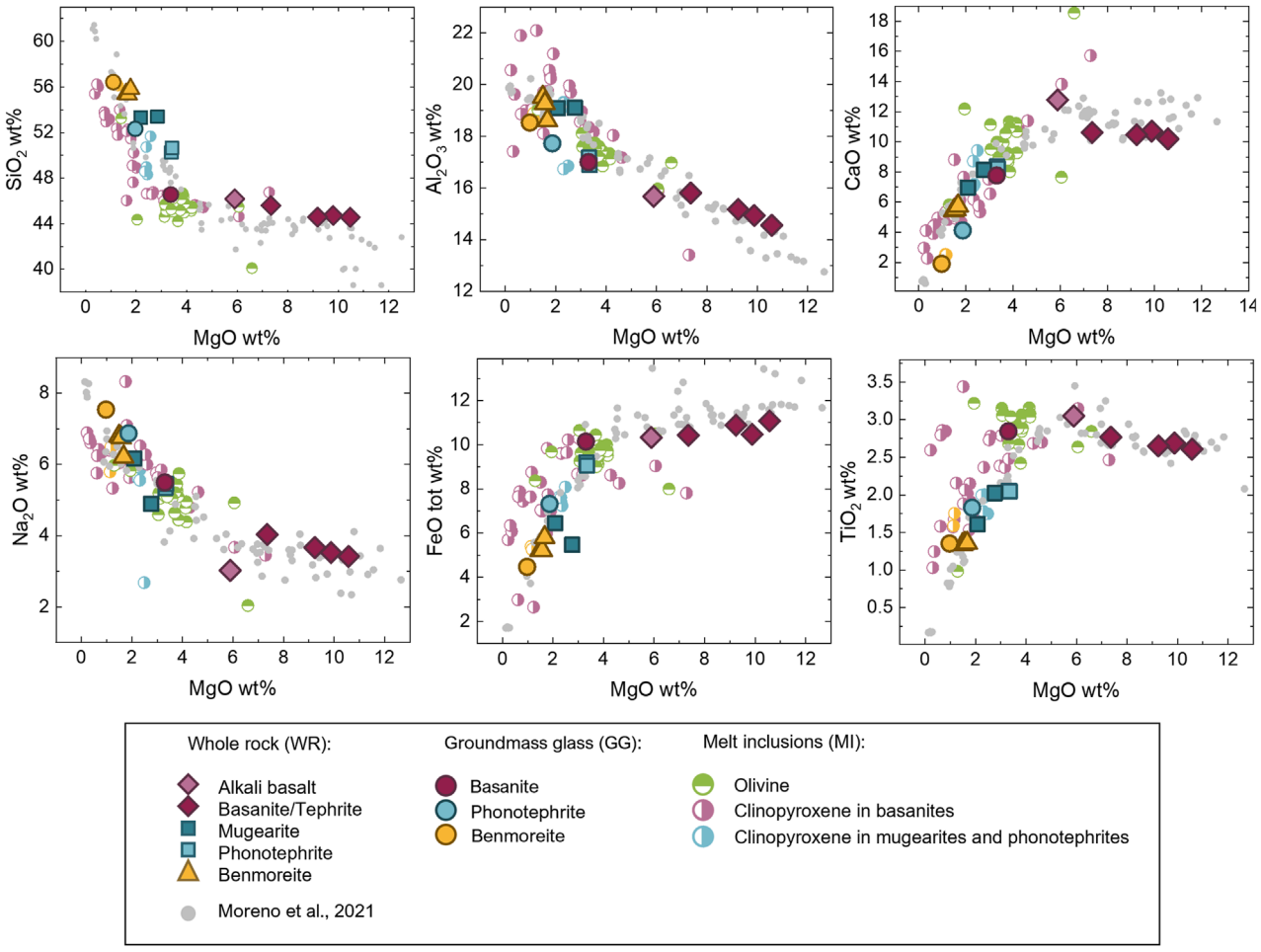

FIGURE 3
Major element vs. MgO plots, showing whole–rock compositions, average groundmass glasses, melt inclusions in olivines and clinopyroxenes of sampled basanites, phonotephrites, and benmoreites of Vesteris Seamount. Filled symbols of diamonds, squares, and triangles represent whole–rock compositions from Beloša et al. (2024); whole–rock compositions of Moreno et al. (2021) sample set are plotted with gray circles; half–filled circles present melt inclusions in olivine and clinopyroxene; filled colored circles represent groundmass glass mean compositions for basanites (SiO_2 47.2 ± 1.7, MgO 3.3 ± 0.8, Al_2O_3 17 ± 1.1, CaO 7.8 ± 2.3, Na_2O 5.5 ± 0.7, FeO_{TOT} 10.1 ± 1.8, TiO_2 2.8 ± 0.5), phonotephrites (SiO_2 52.9 ± 0.8, MgO 1.9 ± 0.4, Al_2O_3 17.7 ± 0.5, CaO 4.1 ± 1.1, Na_2O 6.9 ± 0.4, FeO_{TOT} 7.3 ± 0.5, TiO_2 1.8 ± 0.2), and benmoreites (SiO_2 56.9 ± 0.9, MgO 1 ± 0.3, Al_2O_3 18.5 ± 0.5, CaO 1.9 ± 0.5, Na_2O 7.3 ± 1, FeO_{TOT} 4.5 ± 0.9, TiO_2 1.3 ± 0.3).

resorbed cores that are present in basanites and phonotephrite but absent in benmoreites, as seen in Figure 4; Supplementary Figure S6. In detail, low-Mg cores are MgO, TiO_2 and Cr_2O_3–poor and FeO and MnO–rich (Supplementary Table S4). The low-Mg cores have similar chemistry across our sample set, and the lowest Mg#, $Mg\#_{50–62}$ and $Mg\#_{47–66}$ in basanites and phonotephrites, with low TiO_2 values starting at 0.3 wt%. The low-Mg cores are shown in Supplementary Figures S7–S9, with sharp boundaries with dark mantles and oblate shapes.

In all three rock types, high-Mg mantle portions of clinopyroxene show the highest Mg values ($Mg\#_{78±3}$). High-Mg mantles in basanite–hosted clinopyroxenes have higher concentrations of Cr_2O_3, recording the strongest mafic signature. There are similar, negative trends in Al_2O_3, TiO_2, and Na_2O as a function of Mg#, and positive trends with SiO_2 and Cr_2O_3 (Figure 4). The Cr_2O_3 wt% correlates positively with Mg# in mantles of basanites and, to some extent, phonotephrites, while in benmoreites, this is not the case. In sector–zoned and complex–zoned phenocrysts, hourglass sectors (darker BSE) are richer in SiO_2 and MgO, while prism sectors (brighter BSE) are enriched in Al_2O_3 and TiO_2 (Supplementary Figure S8, S10). This pattern of elemental partitioning between sectors is typical of alkaline magmas (Ubide et al., 2019).

4.3.5 Plagioclase

Plagioclase phenocrysts {$An_{82–36}$; [An = 100 x Ca/(Ca + Na)]} are classified as bytownite, labradorite, and andesine (Figure 5A; Supplementary Table S5). The phenocrysts only occur in benmoreites, where cores, mantles, and rims were analyzed. Groundmass microcrysts from all rock types were analyzed. Benmoreite phenocrysts display oscillatory, patchy, and normal zoning in order of abundance. We performed multiple profile analyses across several phenocrysts, as shown in Supplementary Figure S4.

10.3389/feart.2024.1501694

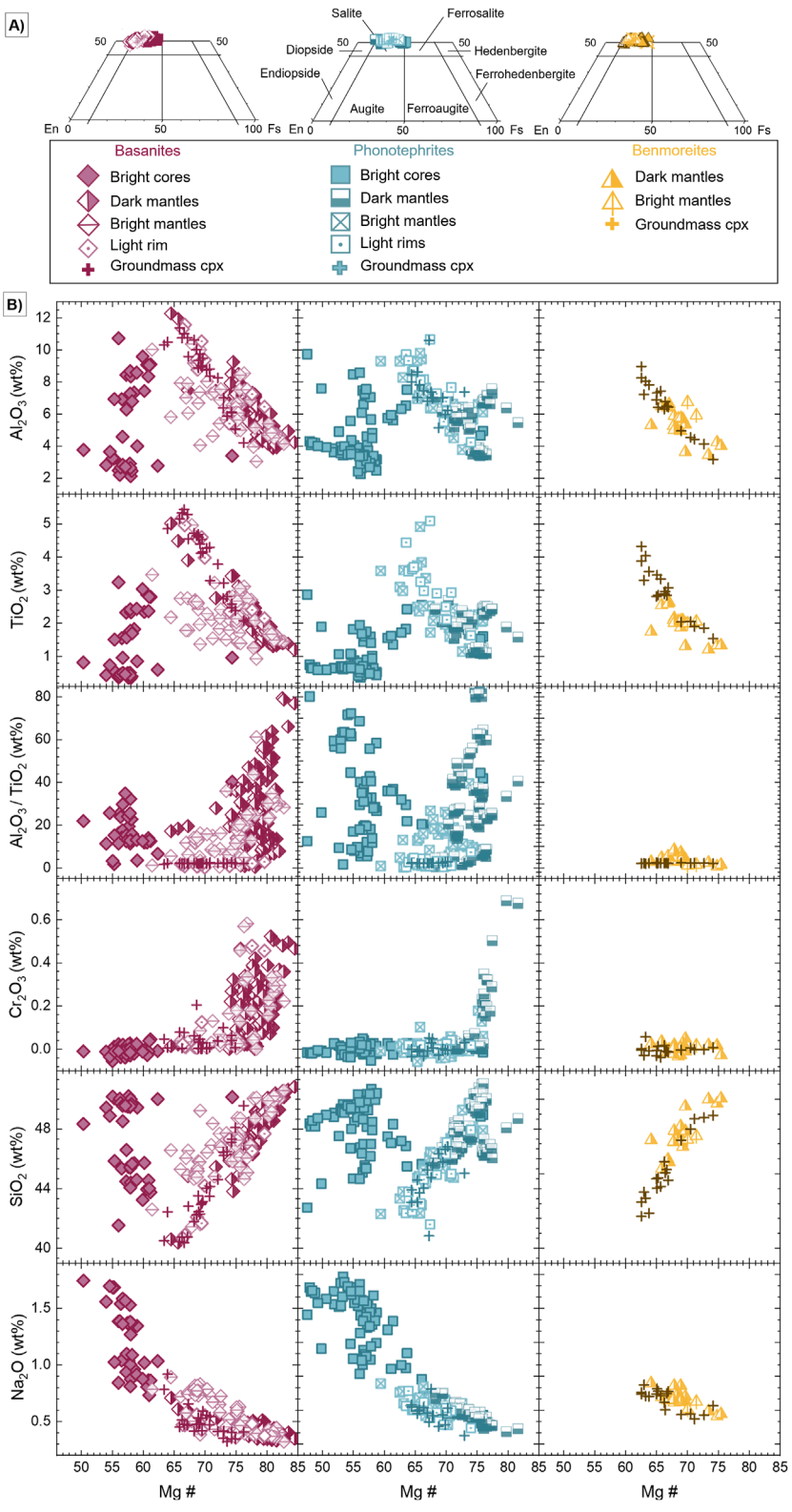

FIGURE 4
Clinopyroxene compositional variations. Colours represent rock type (clinopyroxene in basanites – pink diamonds, in phonotephrites – blue rectangles, in benmoreites – yellow triangles), and symbols fill represent textural characteristics stated in the legend. **(A)** Quadrilateral En–Wo–Fs diagrams for clinopyroxene phenocrysts and groundmass clinopyroxenes from Vesteris Seamount lavas. **(B)** Major element compositions of clinopyroxene phenocryst and groundmass clinopyroxenes. From top to bottom – Al_2O_3, TiO_2, Al_2O_3/TiO_2, Cr_2O_3, SiO_2 and Na_2O versus Mg# (Mg# = 100 Mg/(Mg + Fe_{TOT}), concentrations expressed on a molar basis and Fe_{TOT} representing total iron as Fe^{2+}) of clinopyroxene cores, mantles, and rims and groundmass clinopyroxene.

10.3389/feart.2024.1501694

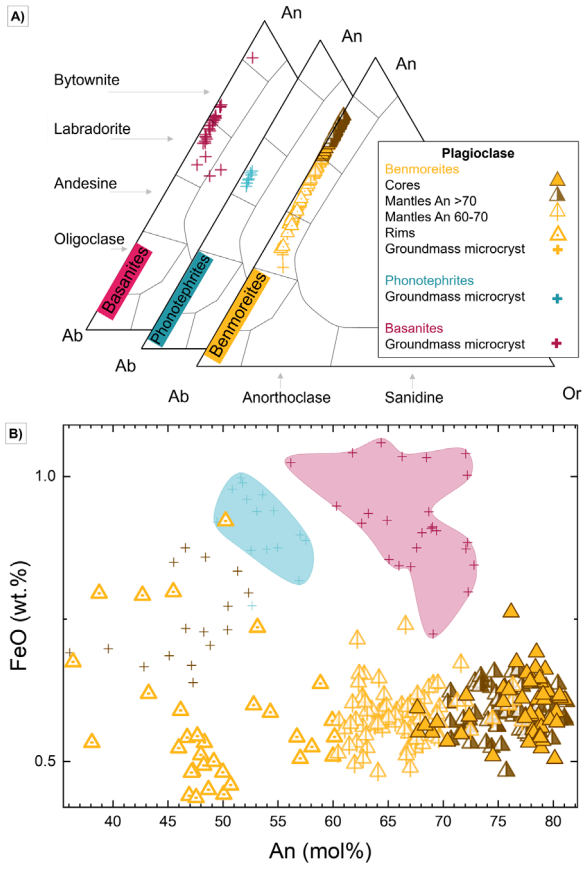

FIGURE 5
(A) Mineral chemistry classification Ternary diagram (Ab–Or–An) for feldspars phenocrysts and groundmass in basanites, phonotephrites, and benmoreites from Vesteris Seamount. **(B)** Fe_{TOT} (total iron as Fe^{2+}) versus anorthite [An = 100 × Ca/(Ca + Na)] content of plagioclase cores, mantles, and rims of benmoreites. Groundmass microcrysts of phonotephrites and basanites are denoted with blue and pink fields, respectively.

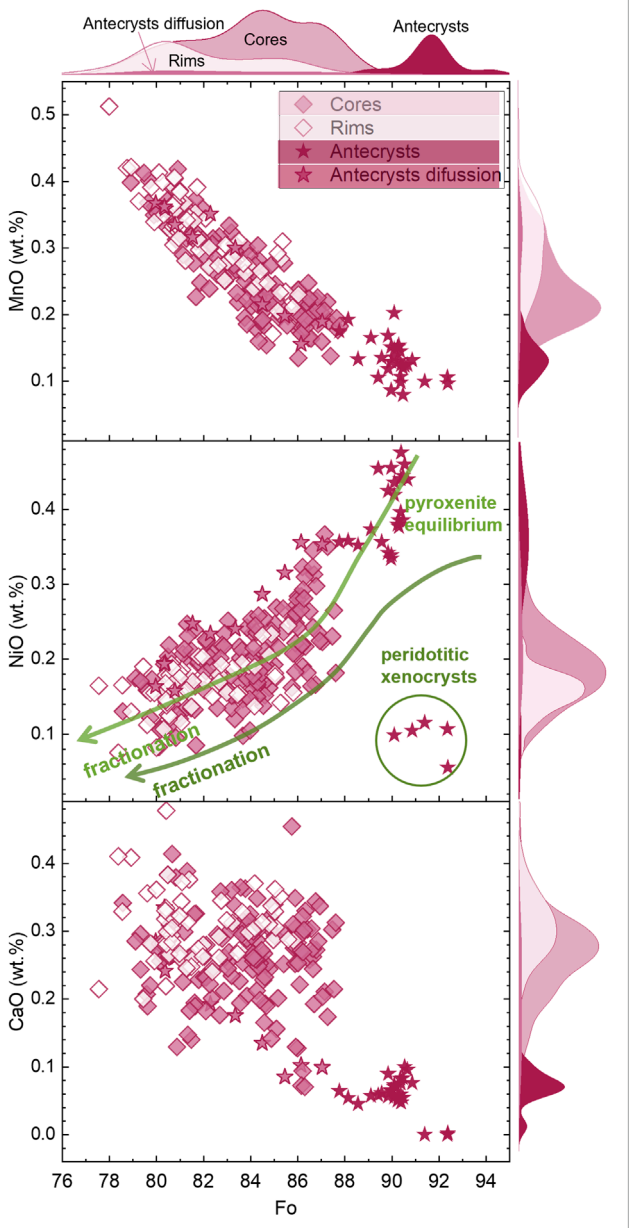

FIGURE 6
Mineral chemistry and classification of olivine from Vesteris Seamount. Graphs contain scatter plots with Kernel distribution estimation curves (KDE) in the margins of the graphs. Top: Mg# vs. MnO (wt%), Middle: Mg# vs. NiO (wt%), and Bottom: Mg# vs. CaO (wt%) plots of olivine. A diagram in the middle represents the fractionation trend for magmas derived from peridotite (dark green curve) and pyroxenite (light green curve) (from (Herzberg, 2011; Sobolev et al., 2005). Olivine ranges in forsterite between Fo92-78.

Plagioclase phenocryst cores have a compositional range of $An_{68–82}$. Core compositions show a bimodal distribution, with the dominant population at $An_{76–82}$ and a minor population in the range $An_{68–75}$. Plagioclase mantles are oscillatory zoned and show complex compositional variations as shown on a 630 μm traverse showing variations between An_{60} and An_{81}(Supplementary Figure S4A). Mantles display dominantly bimodal distributions, with dark mantle zones in BSE contrast having $An_{60–70}$, with few having a slightly higher $An_{60–77}$. Rim compositions vary between An_{36} and An_{60}. The most dominant population is anorthite–poor and clusters around $An_{46–51}$, followed by a population of $An_{52–60}$ and a small group at $An_{36–45}$ (Figure 5B). A general decrease in An from cores (higher CaO) to rims (higher NaO) defines a mild normal zoning pattern overall, with multiple but fine oscillations in An content.

4.3.6 Olivine

Olivine phenocrysts are classified as chrysolite–forsterite [$Fo_{92–78}$; Fo = 100 × Mg/(Mg + Fe_{tot}); (Morimoto, 1988)] (Figure 6; Supplementary Table S6). They occur in one analyzed alkali basalts as fragmented and serpentinized crystals and in basanites as normally zoned crystals with diffusion rims or resorbed olivines with clinopyroxene overgrowth (Supplementary Figure S3A).

Olivine cores range from Fo_{78} to Fo_{92}, with MnO from 0.1–0.4 wt%, NiO from 0.1–0.5 wt%, and CaO from 0–0.4 wt%. Rims overlap with cores, but their ranges begin at higher MnO, lower NiO, and higher CaO (0.2–0.5 wt%; 0.1–0.2 wt%; 0.2–0.5 wt%, respectively). Cores and rims show unimodal distributions and a

strong negative correlation between Fo and MnO, a weak negative correlation between Fo and CaO, and an exponential positive correlation between Fo and NiO, with an outlier cluster having the highest Fo and the lowest NiO (Figure 6).

One outlier cluster corresponds to analyzed glomerocrysts (sample 27) with notably lower NiO and CaO contents and higher Fo than the other phenocrysts (0.05–0.1 wt% and 0–0.1 wt%) (Figure 2D). The olivine glomerocryst shows disequilibrium textures, an exceptional size of >2 mm, and a thick reaction zone (100–200 μm) with decreasing Mg# (Figure 2D). It shows the resorption of olivine on the rims overgrowth with subrounded clinopyroxene crystals (Wo_{40-50}, En_{38-39}, Fs_{10-11}). Adjacent clinopyroxene shows the progressive formation of coalescent clinopyroxenes radially forming a bright halo around dark clinopyroxene. As the growth continues, diffusive re–equilibration modifies zonation.

4.3.7 Amphibole

Amphibole phenocrysts are classified as kaersutite (Leake, 1997). Kaersutites are only occasionally found in basanites, showing reverse zonation without reaction rims. They are often homogeneous but sometimes show oscillatory zoning (Supplementary Figure S3C). The cores have FeO- and MnO–poor compositions (bright BSE), while the rims are MgO–rich, dark BSE defining reverse zoning. In benmoreites and phonotephrites, amphiboles are Mg–rich (MgO up to 13.46 wt%), with medium to low FeO values (FeO from 9.5–18.0 wt%). These kaersutites have a narrow compositional range and significant TiO_2 contents of 3.3–5.8 wt%.

4.3.8 Oxides

Chromium–rich oxides have maximum Cr_2O_3 concentrations of 32 wt% (Cr–spinels), while Ti–rich oxides have maximum TiO_2 concentrations of 43.5 wt% (Ti–magnetites). Oxides occur in glomerocrysts with olivine and clinopyroxene, amphibole, and plagioclase, and as inclusions within the phenocrysts mentioned above. Titanium magnetites are present in more evolved phonotephrites and benmoreites, while Cr–spinels occur in basanites only. Chromium spinels can be zoned with either Cr–poor rims or high–Ti rims that are very bright in BSE (Supplementary Figure S3F5).

4.3.9 Accessory minerals/mineral inclusions

Analyzed apatite occurs as inclusions in glomerocrysts or phenocrysts of amphibole, clinopyroxene, and plagioclase. Analyzed apatite is fluorapatite with mean F and Cl concentrations of 1.4 wt% and 0.5 wt%, respectively, and with high SO_3 abundances (mean SO_3 1.2 wt%) (Supplementary Table S9). On a diagram of Cl contents versus F contents, apatite compositions generate a positive trend with bimodal distribution (Supplementary Figure S11). Apatite with >0.5 wt% Cl are found in plagioclase and amphibole phenocrysts of benmoreites.

Sulfides occur as pyrrhotite ($Fe_{(1-x)}S$) inclusions, with a uniform composition of Fe_{58} S_{38} Ni_1 (Supplementary Table S9). They occur within clinopyroxene, amphibole, and oxides. Alignments of elongated sulfide inclusions follow the orientation of phenocrysts and, in most cases, are not associated with fractures.

Haüyne is a sodalite group, volatile–bearing feldspathoid mineral ($Na_8(AlSiO_4)_6(Cl_2, SO_4)$); (Lessing and Grout, 1971); Supplementary Figure S12). At Vesteris, it is only found in most evolved benmoreites. Elemental data define a slight positive correlation between Na and Si content. Haüyne form Vesteris Seamount is Cl–poor (Cl = 0.2–0.4 wt%), and S–rich (SO_3 = 11.3–14.5 wt%).

5 Discussion

Vesteris lavas provide a record of magma storage beneath the seamount. In the following sections, the pressure–temperature (P–T) conditions of clinopyroxene–melt equilibration were determined to assess the temperature–pressure range of the plumbing system. Then, the petrographic observations and mineral chemistry were combined to assess the origin of different phenocryst populations in alkaline lavas from Vesteris Seamount. Lastly, all the above constraints were connected to reconstruct the architecture of the plumbing system beneath the seamount.

5.1 Pre–eruptive conditions–clinopyroxene thermobarometry

Using thermobarometry on the final growth zones of clinopyroxene phenocrysts, we can reconstruct the P–T conditions of the latest stages of clinopyroxene crystallization before the eruption (Ubide et al., 2023), under the consideration that the equilibrium is reached between the phenocryst mantle and rim compositions and the melts (i.e., whole–rock and groundmass glass compositions). The mantles are typically sector–zoned and have relatively primitive compositions that likely crystallized upon mafic recharge, triggering magma ascent and eruption when the rims formed [as observed at the La Palma 2021 eruption; (Ubide et al., 2023)]. As Vesteris Seamount volcanics are alkaline, we have chosen to apply the clinopyroxene–melt equilibrium thermobarometer of Putirka, (Putirka et al., 1996; 2003; Putirka, 2008), with model uncertainties of ± 27°C and ± 1.7 kbar, 1σ, and where the barometer is temperature and melt–dependent. This model calibration dataset includes various alkaline compositions and is therefore well suited for the Vesteris Seamount's volcanic products. Furthermore, several studies have shown that P–T estimates from this thermobarometer are consistent with depth estimates obtained with different methods such as seismic tomography, seismic reflection profiles, or earthquake patterns in other ocean islands, e.g., (Longpré et al., 2014; Barker et al., 2019; Ubide et al., 2023). As such, the Putirka clinopyroxene–melt thermobarometer has been widely applied in many alkaline settings, e.g., (Klügel et al., 2000; 2005; Nikogosian et al., 2018).

We first selected Vesteris whole–rock compositions from Moreno et al. (2021) with a MgO value of 6 wt% ± 1 to test for equilibrium between these putative liquids and clinopyroxene phenocryst mantles. Moreno et al. (2021) dataset have comparable compositions, but have a wider range in MgO concentrations than our whole rock dataset and are more primitive than the residual glasses analyzed in this study (Figure 3). Therefore, they are more likely to be in equilibrium with the mafic mantles. In

addition, a melt composition with a MgO of 6 wt% minimises crystal accumulation effects, as most OIB liquids erupt at such magnesian value (Ubide et al., 2022). We then tested the use of mean residual glass (groundmass glass) analyses for each sample as putative melts in equilibrium with the clinopyroxene phenocryst rims and mantles hosted in the same sample. Finally, we assessed if melt inclusions hosted in olivines and clinopyroxenes with MgO higher than 6 wt% were in equilibrium with any of the analyzed clinopyroxene compositions in phenocrysts (cores, mantles, or rims).

We performed two tests to assess clinopyroxene–melt equilibrium. The ΔDiHd test (Putirka et al., 1996; Mollo et al., 2013) compares diopside (Di) and hedenbergite (Hd) components observed in the analyzed crystals and those predicted from melt composition. In this test, equilibrium is achieved when ΔDiHd is close to zero (within 10%) (Mollo and Masotta, 2014). We complemented ΔDiHd with the Fe–Mg exchange equilibrium test [Kd Fe–Mg clinopyroxene–melt = 0.28 ± 0.08 (Putirka, 2008)]. Only mineral–liquid pairs that meet these two criteria were considered for P–T assessment (Figure 7). To convert pressure results to depth, we used ($P = d \times \rho \times g$), which represents the fluid's formula for pressure (P). We multiplied the depth (d – represents the height of the fluid column) by the density (ρ – represents the density of the fluid) and acceleration due to gravity (g) to calculate pressure from depth. Given that most of the pressure comes from the crust and uppermost mantle, we used the density of the ocean crust until the Mohorovičić (Moho) discontinuity [crust-mantle boundary in the study area is ~10 km (Voss et al., 2009; Haase et al., 2017)] and uppermost mantle using the most recent density model for the study area (Gómez Dacal et al., 2023) with an average crustal density for the region of 3,000 kg/m^3.

Thermobarometric results from clinopyroxene mantles paired with whole–rock, filled symbols in Figure 7, together with rims paired with matrix glass compositions, hollow symbols in Figure 7, are provided in Supplementary Table S4. Clinopyroxene–melt equilibrium calculations yield pressure and temperature estimates of 6.3 kbar ± 1.2°C and 1130°C ± 39 (average, ±1σ, Supplementary Table S4). The linear P–T arrays are mainly controlled by the thermodynamic principles underlying the thermobarometry models (Putirka, 2008), and we use average ± 1σ values to acknowledge the uncertainty in the models and the analytical data (Wieser et al., 2023). The location of distinct P–T arrays at distinct temperatures is mainly controlled by the choice of equilibrium liquid, e.g., (MacDonald et al., 2023).

In detail, P–T results for the mantles imply final storage at upper mantle conditions. The clinopyroxene mantles of basanites and phonotephrites in equilibrium with whole–rock compositions return the largest range in estimated pressures (9–2 kbar) over a narrow range of temperature (1112°C–1165°C) (Figure 7). Their mean pressure is of 6.4 kbar ± 1.1, coupled to a mean temperature of 1147°C ± 10. The averaged calculated depth for basanite and phonotephrite clinopyroxene mantles – whole–rock pairs corresponds to 22 km. A notable characteristic of the negative trend (Figure 7) defined by these pairs is a small cluster represented by a basanite sample with the highest pressure (8.9 kbar) and temperature (~1160°C). We interpret this to potentially reflect a deep magma reservoir beneath Vesteris corresponding to ~30 km.

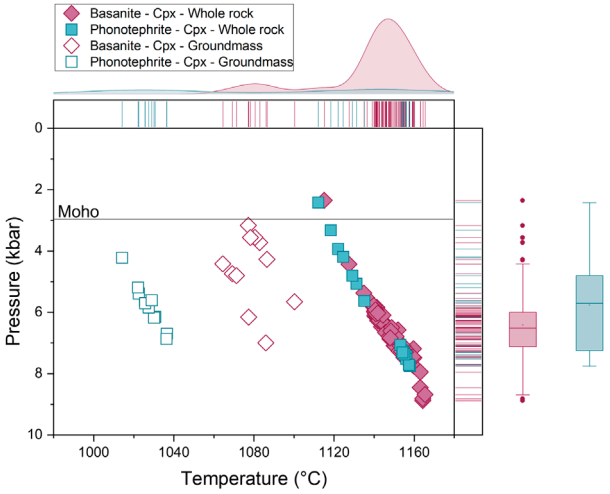

FIGURE 7
Clinopyroxene thermobaromerty using the equation from (Putirka et al., 2003) (temperature and melt–dependant, ±1.7 kbar, 1σ; ±27°C, 1σ). Combined marginal plot with Kernel density estimations (KDE) on the X–axis and box chart with error bars and outliers on the Y–axis of the scatter plot. Clinopyroxene mantles were paired with whole–rock compositions (filled symbols), and clinopyroxene rims were paired with groundmass glasses (empty symbols) as putative equilibrium liquids. Only results that pass mineral–melt equilibrium tests are shown (Supplementary Table S4). Clinopyroxene show a pressure span from 8.9 kbar to 2.4 kbar (~30–8 km), with basanites occurring first at the greatest pressures. Rim equilibration temperatures are much lower for comparable pressure ranges. The black line represent Moho discontinuity.

Clinopyroxene outermost rims, occupying the last ~30 μm of phenocrysts, were paired with groundmass glass compositions from each sample to calculate the final pressure of crystallisation upon magma ascent. As shown in Figure 7, results from basanite clinopyroxene rims – groundmasses form two distinct P–T trends, whose pressures overlap, within method error (7.0–3.2 kbar). Considering the notable overlap between clinopyroxene rims-groundmass P-T results in phonotephrites and basanites, results were averaged and yielded, taken together, 5.2 kbar ± 1.1°C and 1053°C ± 28. In terms of depth, this translates to an averaged depth of 18 km, which is shallower than that of whole–rock – mantle pairs, as expected from the fact that the mantles record crystallisation upon final storage and the rims record final clinopyroxene crystallisation during ascent to eruption. We note clinopyroxenes from the more evolved benmoreites did not pass the equilibrium tests. A simple hypothesis to explain this is that the basanite and phonolite magmas are end–member compositions that crystallize clinopyroxene, while the benmoreites are hybrid melts between the two compositions. Textural evidence of resorption and precipitation in clinopyroxene and plagioclase indicate open system behaviour with magmatic recharge and hybridisation, which is consistent with the protracted volcanic activity of Vesteris seamount, as observed elsewhere, e.g., (Iyer et al., 2012).

Finally, several melt inclusion data with more than 5.9 wt% MgO were not in equilibrium with clinopyroxene compositions from the same samples. However, random pairs of melt inclusion–clinopyroxene were found to be at equilibrium, regardless

of the rock sample or rock type. For example, we found some melt inclusions in phonotephrite clinopyroxenes which were in equilibrium with basanite clinopyroxenes. On the other hand, some melt inclusions in basanite clinopyroxenes were in equilibrium with some clinopyroxene compositions from basanites and phonotephrites. We note that the equilibrium melt–clinopyroxene does not appear to hold to particular areas of the crystal. The mean pressure inferred from these melt inclusions–clinopyroxene equilibrium calculations is 5.3 ± 0.9 kbar. Although the P–T estimates obtained from pairing melt inclusions with the clinopyroxenes are inconsistent, the calculated pressures encompass the range (depths of 17–26 km) registered by other pairs (i.e., rims/mantle – groundmass glass/whole–rock) and could imply phenocryst formation and melt inclusion entrapment during storage in the upper mantle.

5.2 The origin of the bright BSE cores

Clinopyroxene cores are low-Mg and show patchy resorbed corroded textures, rounded morphologies, and sharp boundaries with surrounding high-Mg mantles, which is regarded as a strong signal of magmatic open systems involving mafic recharge and mixing (Streck, 2008; Ubide et al., 2023; Jankovics et al., 2013; Soltanmohammadi et al., 2021; Ziem à Bidias et al., 2021; Dobosi and Fodor, 1992; Pilet et al., 2002); Figure 2, Supplementary Figures S2, S3.

Low-Mg cores are mostly not in equilibrium with whole–rock compositions nor with groundmass glasses, and do not form coherent fractionation trends with the remaining clinopyroxene data (Figure 4). The low-Mg cores have the lowest Mg# contents in our dataset, together with consistently low Cr_2O_3 and high Na_2O concentrations (Figure 4). In most clinopyroxenes in all rock types, from low-Mg cores to high-Mg mantles, TiO_2 rises, except in one reverse–zoned clinopyroxene in basanites (Supplementary Figure S7B).

The low Mg# contents suggest crystallisation from evolved magmas. The Mg# values are too low to be derived from typical mantle peridotites, and the lower Al_2O_3, TiO_2 while higher SiO_2 concentrations relative to the main fractionation trend defined by mantles and rims suggests a separate origin (Figure 4). We interpret the low Mg# cores to represent antecrysts from evolved, cooling mushes recycled by primitive recharge melts with higher Cr contents (Streck, 2008; Yang et al., 2023; Ubide and Kamber, 2018). As mafic injections are recharging the system, crystallization of the main clinopyroxene fractionation trend happens upon recharge, mixing, and ascent [as observed in other alkaline settings, e.g., La Palma; (Ubide et al., 2023), Petpenoun volcanoes; (Ziem à Bidias et al., 2021), Dahongliutan volcanic rocks (Yang et al., 2023)]. While thermobarometric estimates on the cores are hindered by the lack of equilibrium with melt compositions, their Cpx overgrown have necessarily crystallized at upper mantle conditions, as demonstrated earlier (section: Pre–eruptive conditions – Clinopyroxene thermobarometry).

Interestingly, as shown in Figure 6, olivine data, both petrographical and mineralogical, reveal the occurrence of refractory, high forsterite (Fo) Olivine antecrysts (>90), which might originate either from pyroxenitic or peridotitic sources (Sobolev et al., 2005; Straub et al., 2008; Herzberg, 2011). When coupled to low Ni (0.34–0.50 wt%) (samples 5, 14, 94–1), low CaO and high Fo contents (Figure 6), such refractory compositions might be representatives of cratonic mantle relics rather than simple residues of the asthenosphere. Olivine with a Fo content greater than 92 cannot be normally produced during mantle melting [e.g., (Arndt et al., 2009)]. In addition, most olivines from Archean cratons have high–Fo contents [89–95; e.g., (Arndt et al., 2009; Liu et al., 2022)], while those of the convecting mantle have lower Fo contents of 88–93. Such high–Fo olivines are possibly derived from Archean depleted lithospheric domains, which might have been thermally eroded by the Icelandic plume, as suggested by (Beloša et al., 2024). The same might hold for the pyroxenites, as sublithospheric mantle domains might be veined with cm–scale pyroxenite heterogeneities (Straub et al., 2008). However, it is unclear if these antecrysts are assimilated within the upper mantle during melt transport or during melt recharge of low Mg# clinoypyroxene mushes.

5.3 Origin and implications of phenocryst textural and compositional zoning

We use mineral chemistry from Vesteris Seamount to explore the magmatic processes recorded by clinopyroxene (Davidson et al., 2007). Focusing on clinopyroxene allows us to explore crystallization processes inside the plumbing system over a wide P–T range, with slow elemental diffusion at the lattice scale (Streck, 2008; Ubide and Kamber, 2018; Ubide et al., 2019). Based on micro–analytical techniques and zoning patterns, we investigate the stages and crystallization history of Vesteris lavas. Most of the phenocrysts are zoned, but they exhibit different textures and zoning patterns across the studied sample suite (Figure 8), which are described below and are taken to reflect magmatic system complexity.

Normal zoning (i.e., decreasing Mg concentration from core to rim) implies compositional core–rim changes induced by changes in the melt composition during cooling and fractionation. Normal zoning is present but is the rarest zonation pattern observed in Vesteris lavas. In some phenocrysts, zonation progresses smoothly from core to rim (Supplementary Figure S6A). In most others, it is represented by an abrupt change in major element concentration with a sharp boundary (Supplementary Figure S6B).

Ubiquitous glomerocrysts, which are composed of multiple clinopyroxenes bound together surrounding the largest clinopyroxene phenocrysts in basanites, show normal zoning as well (Supplementary Figure S4). Glomerocryts show multiple zonation types. As an example, small clinopyroxenes of second–generation surrounding main phenocrysts show complex zoning, such as a mixture of oscillatory and sector zoning (Figures 2, 8, 9; Supplementary Figure S5).

Reverse zoning implies compositional inversions from what would be expected to result from crystallization in a closed system (Streck, 2008). Reverse zoning is the most common type within the Vesteris lavas. This type of zoning is recorded in various volcanic rocks [e.g., (Svetov et al., 2020; Tapu et al., 2022)] and is considered to record processes in an open system, which implies magma mixing and mingling (Kamacı and Altunkaynak, 2019; Streck, 2008). Very

10.3389/feart.2024.1501694

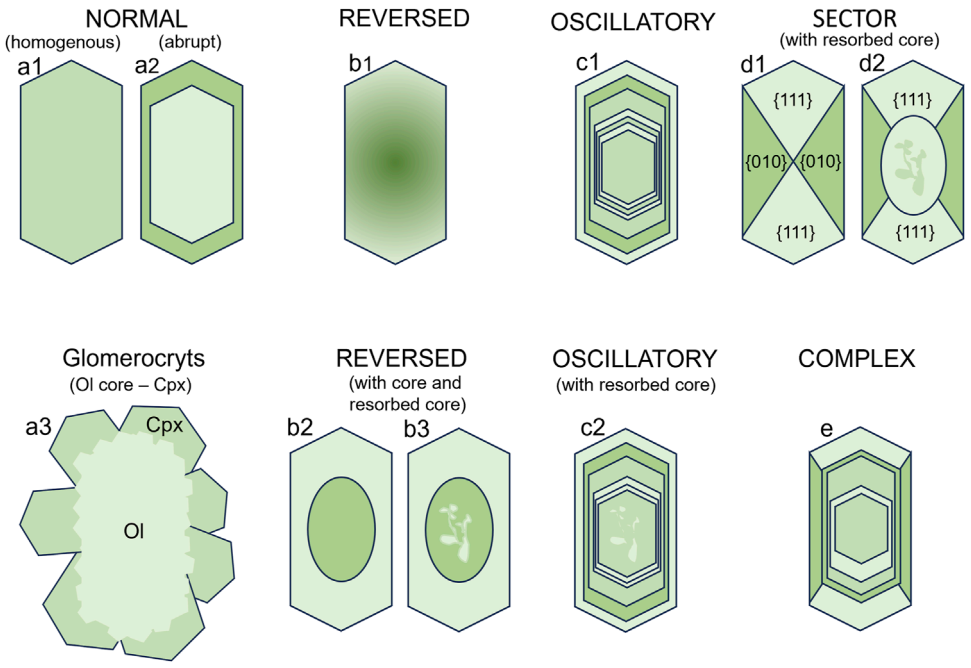

FIGURE 8
Schematic illustrating zonation types present in clinopyroxene of Vesteris Seamount lavas. Colors, especially green cores (bright in BSE images), are as seen with PPL. The clinopyroxene zoning patterns can be divided into distinct types within the lava suite: **(A)** normal zoning: 1 – homogenous, 2 – with a single, abrupt change in major element concentration with a sharp boundary, 3 – glomerocrysts; **(B)** reversed zoning: 1 – progressive–small variations in major element contents, 2 and 3 – with a distinct bright BSE core that in some case show resorption textures; **(C)** oscillatory zoning is mostly present in phenocrysts with resorbed, cellular textured cores; **(D)** sector zoning with BSE dark hourglass sectors; **(E)** complex zoning – a combination between sector and oscillatory zonation.

often, resorption textures are found in reversely zoned phenocrysts. It is defined by an increase in Mg#, TiO_2, and Cr_2O_3 and a decrease in MnO from the center to the margins (Supplementary Figure S7). Diffuse, progressive zoning that produces smooth analysis profiles is extremely rare in reverse–zoned phenocrysts. Still, one example is found in fragmented phenocrysts of basanite (sample 14) with a slow Mg# increase from 75 to 80 (Supplementary Figure S7A). Reversely zoned phenocrysts with low-Mg cores (discussed in Section 5.2) are the most common ones. Low-mg resorbed cores are characterized by a sharp boundary with the surrounding mantle. They have extremely low Cr_2O_3 contents – and plot outside the main clinopyroxene differentiation trends, also observed elsewhere (e.g., Cape Verde (Eisele et al., 2016), Canary Islands (Barker et al., 2015); Supplementary Figure S13). Cores do not show the same correlations with the Mg# as mantles and rims do (e.g., for Al and Ti contents, cores show a slight positive and for mantle a negative correlation with Mg#; Figure 4). As a whole, these observations are consistent with the low-Mg cores being antecrysts in origin.

Elemental decoupling is also observed in the sector–zoned clinopyroxenes (Supplementary Figure S8). Clinopyroxenes showing sector zoning have two distinguished forms, hourglass (basal) −111 and prism form 100, 110, and 010 (Ubide et al., 2019). Hourglass sectors are darker in BSE images; most notably, this reflects Mg enrichment relative to Fe–Al–Ti–rich prism sectors (Supplementary Figure S8). The presence of sector zoning in clinopyroxenes suggests crystallization upon ascent after injection of mafic melt, in this study presented by low-pressure clinopyroxene-whole rock measurements on Figure 7 (MacDonald et al., 2023; Ubide et al., 2019; 2023). The presence of relatively evolved antecrysts suggests magma recharge events and magma mixing during upper mantle storage, as observed in other OIB settings (Ubide et al., 2019). This is also supported by thermobarometric calculations indicating polybaric crystallization ranging from ~9 to 2 kbars (Figure 7).

Oscillatory zoning is defined by a succession of distinct compositional layers generally parallel to crystallographic planes (Shore and Fowler, 1996). These zonations are recognizable on BSE images due to alternating concentric zones with different grey shades (Supplementary Figure S9). Their variable thicknesses record different growth rates for distinct crystal areas. Oscillatory zoned mantles toward the rims display fractional crystallization trends with decreasing Mg# and FeO content and increasing TiO_2 content (Supplementary Figure S9). Complex zonation combines sector and oscillatory zoning (Supplementary Figure S10) and can be present in clinopyroxenes with and without resorbed cores.

5.4 Architecture and processes within the plumbing system

Based on the above thermobarometry and mineralogical observations, we propose a magmatic system model for Vesteris

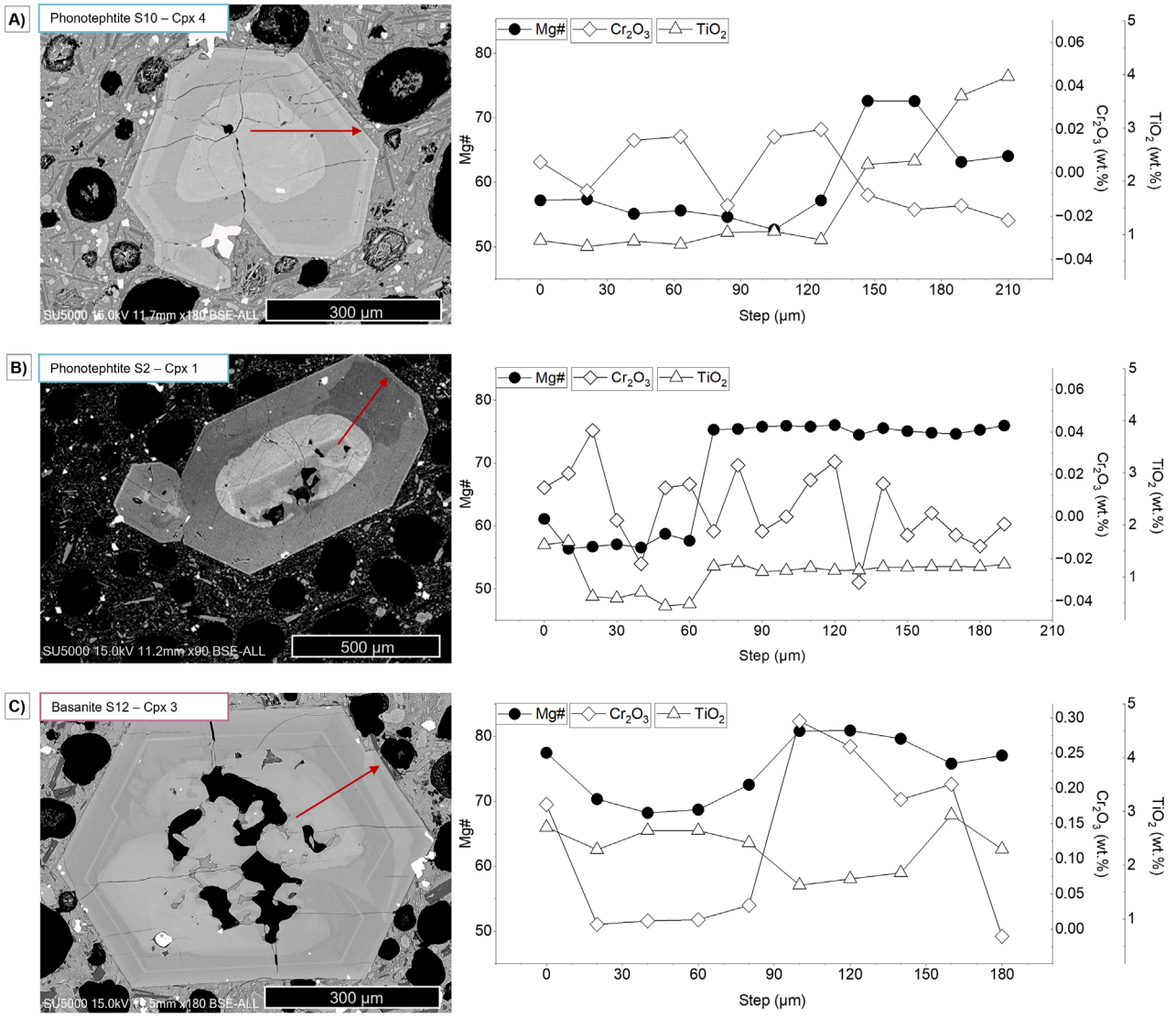

FIGURE 9
Analyzed traverses of clinopyroxene phenocrysts in phonotephrites and basanite marked on BSE images with a red arrow. The X–axis represents measured step in μm, while Y–axis represents Mg# (left) and TiO_2, Cr_2O_3 (right). **(A)** reversely zoned euhedral clinopyroxene with subhedral core, **(B)** reversely zoned euhedral clinopyroxene with pronounced sector zoning (hourglass sector darker in BSE), and anhedral resorbed core, **(C)** euhedral, reversely zoned clinopyroxene with highly resorbed anhedral core and oscillatory zoned mantle. Generally, low–Mg resorbed cores are followed by high–Mg recharge mantles and low–Mg diffusion rims.

Seamount (Figure 10). Vesteris stands in the Greenland Basin, approximately 3,088 m above the seafloor (Moreno et al., 2021). The sediment coverage of Greenland Basin overlies relatively old 40.3–43.4 Ma ocean crust (Gaina et al., 2009; Zhang et al., 2020). Sitting atop is Vesteris seamount associated with a crustal thickness of ~10 km (Voss et al., 2009; Haase et al., 2017).

Thermobarometric calculations indicate that the crystallization of Vesteris alkaline lavas is polybaric, with pressures varying from 8.9 to 2.4 kbar. Associated temperatures vary as a function of the equilibrium liquid composition between 1014°C and 1100°C for residual glasses and more than 1112°C for mean whole–rock compositions. Mean crystallization pressures are 6.4 ± 1.1 kbar and 1140 ± 34°C for basanites (n = 96) and 5.9. ± 1.4 kbar and 1095 ± 59°C for phonotephrites (n = 27). Such a pressure range indicates the existence of a magma mush system rooted within the lithospheric mantle beneath Vesteris at 15–30 km depth. Indeed, magmas derived from the deep Iceland mantle plume source (Beloša et al., 2024) probably ascend through the thick oceanic lithospheric mantle [mean lithospheric thickness 50 km (Steinberger and Becker, 2018)], up to be stalled beneath the oceanic crust (Voss et al., 2009). Major fractionation of magmas occurring within the uppermost mantle has also been reported at Cape Verde, Crozet, Kerguelen, Madeira, and Canary Islands, e.g., (Amelung and Day, 2002; Damasceno et al., 2002; Schwarz et al., 2004; Longpré et al., 2008; Meyzen et al., 2016). Similarly, combined studies of thermobarometry and mineral chemistry globally suggest that crystallization at some seamounts

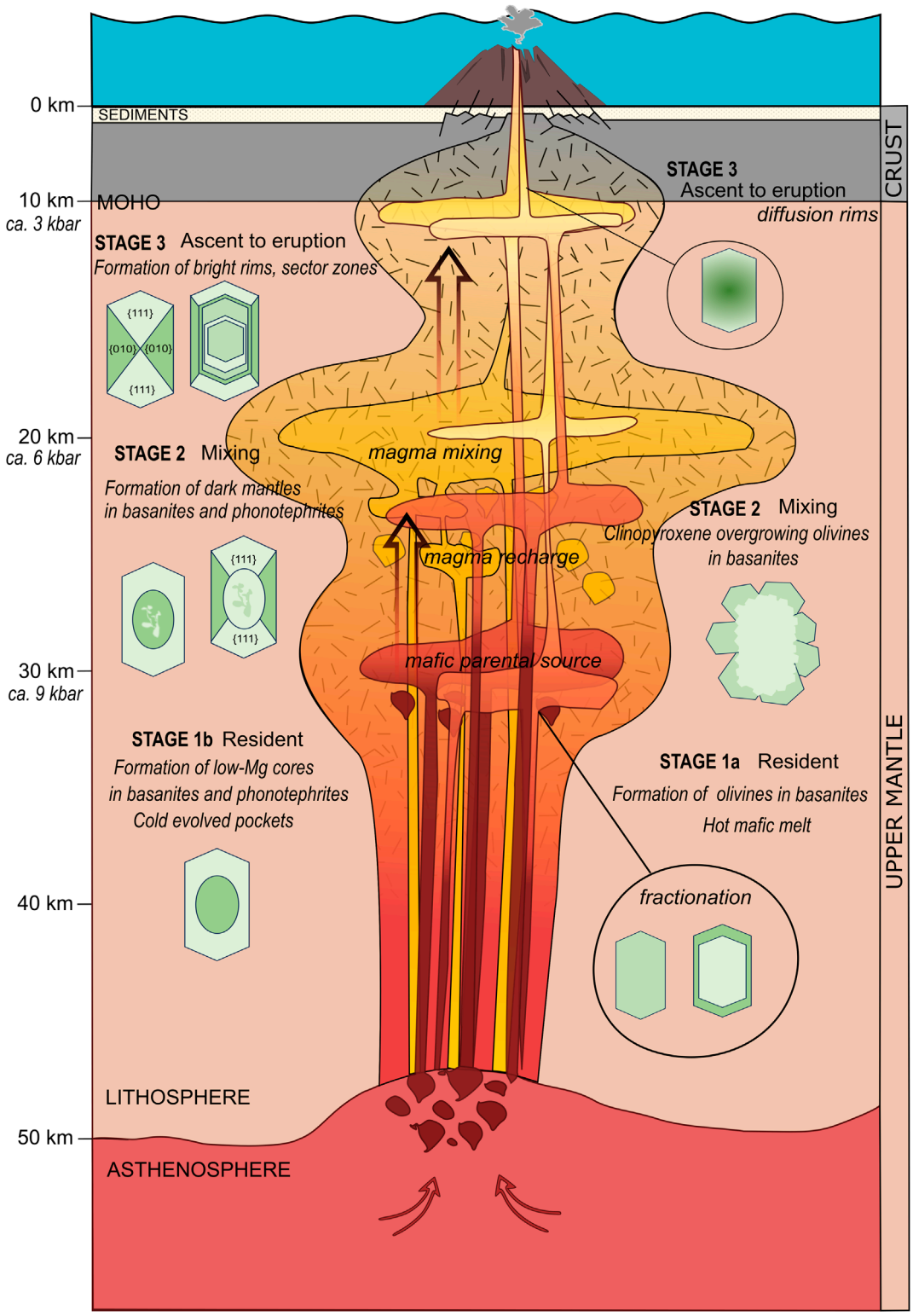

FIGURE 10
A simplified schematic model of the evolution of the magmatic system for the Vesteris Seamount in the Greenland Basin. The figure shows a magma ascent, storage, and recharge model at different depths within the oceanic lithosphere below the base of the oceanic crust. Illustrated phenocrysts show clinopyroxene and their zonation types correspond to Figure 8. The figure illustrates three main stages that formed 1) green cores (bright with BSE contrast) with low Mg# formed from relatively evolved mafic melt, 2) light green mantles (dark with BSE contrast) with high Mg# grew surrounding the cores from a more primitive melt entering the system, and a final stage 3) that formed thin diffusion rims around clinopyroxenes upon ascent. Figure not to scale.

occurs at upper mantle depth (e.g., Cape Verde (Barker et al., 2012; 2019)). Recent thermodynamic modeling has shown that fractionation from parental OIB melts can generate fractionated magmas with 5wt% MgO in the upper mantle preferentially erupts due to volatile saturation (Ubide et al., 2022). Magmas with 5wt% MgO dominates the compositional array of many OIB systems, with limited or no crustal storage (Klügel et al., 2015; Dayton et al., 2023).

Our new results also show that fractionation of evolved rocks, such as phonotephrites, can occur in the lithospheric mantle, as defined by clinopyroxene–melt pairs. While some sector zoned clinopyroxenes crystallized at a shallower crustal level (19–8 km), either during transport towards the surface or in shallower magmatic lenses beneath Moho (Figure 10), high-Mg mantles are crystalized at deeper levels corresponding to 30–19 km (Figure 7; Supplementary Table S4). The difference in the temperature range obtained using compositions of residual glasses and mean whole–rock compositions can be accounted by the presence of magma bodies of different sizes at similar depths having distinct temperature regimes due to variable cooling times and injection frequencies (Figure 10). Indeed, phenocryst textural and mineralogical characteristics of both clinopyroxene and plagioclase, the latter being only found in benmoreites, suggest that deep, lithospheric mantle magma reservoir, storing moderately fractionated melts that undergo periodic recharge by primitive melts, triggering the transport and assimilation of antecrysts of clinopyroxene and olivine at shallow levels (Figure 10). Evidence for injection events is provided by a) recycled, patchy, and spongy cores of antecrysts, b) mixing and formation of zoned clinopyroxene overgrowth over olivine cores in basanites, c) dissolution of skeletal olivine phenocrysts in basanites, and d) growth of high-Mg mantles around partially resorbed low-Mg cores in clinopyroxene in basanites and phonotephrites. In addition, clinopyroxene overgrowths with high-Mg mantles suggest cogenetic growth (Villaseca et al., 2020) but different degrees of maficity/evolution. This is also observed in high-Mg euhedral clinopyroxenes displaying overgrowths over the large population of olivines, which typically have the highest Mg (higher than Mg#83) compared to the bright mantles with Mg# 70–83. Mafic recharge led toward resorption of the pre–existing cores and more mafic clinopyroxene mantles and clinopyroxene growth around olivine phenocrysts; This population of clinopyroxene is characterized by prism and hourglass sectors. Prism sectors accommodate Ti–Al enrichment and follow typical partitioning in other alkaline systems (MacDonald et al., 2023; Ubide et al., 2019; 2023). The low-Mg core population possibly crystallized within the cold evolved melt pockets at high–pressure (Tapu et al., 2022; Villaseca et al., 2020; Ubide et al., 2019). Benmoreitic clinopyroxene is equilibrated neither with whole–rock nor with groundmass glass compositions; consequently, benmoreites are considered to represent hybrid melts. In addition, the lack of antecrysts as well as the ubiquitous normal zoning of clinopyroxene, lead us to conclude that haüyne–bearing benmoreites represent a late crystallization stage that evolved from phonotephrite – basanite magma. Although we cannot assess the depth of crystallization, the presence of plagioclase phenocrysts may suggest the involvement of localized shallower storage at the crustal/Moho level, enhancing degassing–induced crystallization.

5.5 Comparison with other seamounts

Vesteris shows strong coherence with the global seamount dataset, based on the petrology, mineral chemistry (i.e., clinopyroxene), and whole–rock geochemistry of other off–axis seamounts [i.e., Capo Verde (Barker et al., 2012), and Comoros archipelago (Berthod et al., 2021)] (Supplementary Figures S13, S14). However, Vesteris whole–rock data plot at moderately high Al_2O_3 for a given MgO, relative to other seamounts, reflecting a lower amount of plagioclase fractionation at this location relative to the majority of seamounts investigated to date. This may imply higher water content in the Vesteris magma that suppresses plagioclase fractionation and leads to early clinopyroxene crystallization (Danyushevsky, 2001; Michael and Chase, 1987), and would be consistent with the presence of amphibole phenocrysts. Alternatively, it could reflect the presence of a thick lithospheric lid under Vesteris, which led to a greater depth of initial fractional crystallization below the depth of plagioclase stability in basaltic melts (Feig et al., 2006). There is growing evidence from geophysics observations and thermobarometry, e.g. (Ubide et al., 2022; Dofal et al., 2022; Ma et al., 2024; Dragone and de Souza Bologna, 2024), that magma plumbing system extends into the lithospheric mantle under seamounts and oceanic islands. Our results and studies on mineral assemblage and P–T thermobarometry on clinopyroxene phenocrysts indicate that evolved magmas, with lower Mg# than in equilibrium with typical mantle olivine, can evolve in these lithospheric mantle plumbing systems.

6 Conclusion

To determine pre–eruptive processes and plumbing system architecture at Vesteris, the largest seamount in the NE Atlantic Ocean, we investigated textural and geochemical patterns in the crystal cargo of a suite of Vesteris dredged volcanic rocks. Clinopyroxene zoning holds the richest record of pre–eruptive history, given its stability across a range of depths, temperatures, and water content, and its common occurrence in Vesteris lavas. Other phenocrysts with high modal % are plagioclase, olivine, amphibole, Fe–Ti oxides, and accessory minerals. Clinopyroxene phenocrysts commonly host resorbed, low-Mg cores that are interpreted as the products of crystallization of evolved magma pockets at upper mantle conditions. Overgrowth mantles in the same rocks show dark BSE contrasts and mafic compositions that reflect crystallization from the eruption–triggering mafic recharge melts during final storage in the upper mantle, while evolved rims are assumed to reflect the onset of magma cooling upon ascent or possibly while stored beneath Moho.

Thermobarometric investigations of clinopyroxene–melt equilibrium pairs constrain polybaric upper mantle storage conditions. Groundmass glass compositions paired with clinopyroxene rims return the shallowest depths (basanites 4.6 kbar ± 1.2 kbar; 1097°C ± 10°C; phonotephrites 5.8 kbar ± 1.0 kbar; 1027°C ± 7°C), while whole–rock compositions paired with clinopyroxene mantles reflect crystallisation at higher pressures and temperatures upon mafic recharge and mixing (basanites: 6.6 kbar ± 0.9 kbar; 1148°C ± 8°C; phonotephrites 6 kbar ± 1.8 kbar; 1142°C ± 16°C). These pressures correspond to storage at ~8–30 km

depth. While thermobarometric constraints in low-Mg cores are hampered by the lack of equilibrium liquids, we infer crystallisation at upper mantle conditions based on their textural relationship with overgrowth high-Mg recharge mantles. Based on these data, we infer that clinopyroxene crystallization started at about 8.9 kbar for basanites and 7.8 kbar for phonotephrites and continued until magma eruption at the surface.

Combining mineral zoning and thermobarometric constraints, we define three distinct stages of magmatic evolution: (1) formation of low-Mg cores from cold, evolved crystal–melt mushes, olivines from hot and mafic melts, and clinopyroxenes phenocrysts, crystalized at max. 8.9 kbar, 1160°C, ~30 km, (2) magma mixing in a shallower chamber upon mafic recharges (4.3–7.4 kbar, 1000°C–1160°C, ~14–25 km), (3) ascent to eruption and formation of low-Mg rims around Moho depths. Based on clinopyroxene geochemical data and textural descriptions, we postulate the model we propose for Vesteris magma plumbing architecture may be applicable to other OIB type settings that erupt through moderately thick lithosphere elsewhere.

Data availability statement

The original contributions presented in the study are included in the article/Supplementary Material, further inquiries can be directed to the corresponding author.

Author contributions

LB: Conceptualization, Formal Analysis, Investigation, Methodology, Software, Visualization, Writing–original draft, Writing–review and editing. DM: Supervision, Validation, Writing–original draft, Writing–review and editing. TU: Supervision, Validation, Writing–review and editing. SC: Conceptualization, Writing–review and editing. CM: Writing–review and editing. MB: Writing–review and editing. AM: Conceptualization, Resources, Writing–review and editing.

Funding

The author(s) declare that financial support was received for the research, authorship, and/or publication of this article. We acknowledge financial support from the Research Council of Norway (NFR) through its Centers of Excellence scheme, project number 223272 (CEED) and project number 332523 (PHAB). LB acknowledges additional support from NFR through project NORRAM 30947. SC acknowledges funding from the NFR Young Research Talent Grant 301096. AM acknowledges NFR support through the HOTMUD (project number 28829) and NCS2030 (project number 331644). TU was supported by an Australian Research Council Future Fellowship (ARC FT230100230; RM 2023000028).

Acknowledgments

We acknowledge the Volcanic Basin Petroleum Research (VBPR) and TGS Norway, with special thanks to Stephane Polteau and Sverre Planke for organizing the survey and kindly providing the samples. We acknowledge and thank Carmen Gaina and project NORRAM 309477 for sample analysis funding. We acknowledge Marco Acavedo Zamora for contributing to this publication by providing scanned thin sections of Vesteris Seamount. Furthermore, we are deeply thankful to Muriel Marie Laure Erambert at the Department of Geosciences, UiO, for all the help and guidance with the electron probe microanalysis of the phenocryst assemblage of Vesteris Seamount. We thank Wolfgang Bach, Karsten Haase, Cristoph Beier, and Colin Devey for their collaboration and for providing multibeam bathymetry data for Vesteris Seamount. We thank Ian Ernest Masterman Smith and May (Mai) Sas (PhD) for thorough review, which significantly improved this article.

Conflict of interest

The authors declare that the research was conducted in the absence of any commercial or financial relationships that could be construed as a potential conflict of interest.

Publisher's note

Supplementary material

The Supplementary Material for this article can be found online at: https://www.frontiersin.org/articles/10.3389/feart.2024.1501694/full#supplementary-material

References

Acevedo Zamora, M. A., and Kamber, B. S. (2023). Petrographic microscopy with ray tracing and segmentation from multi-angle polarisation whole-slide images. *Minerals* 13, 156. doi:10.3390/min13020156

Amelung, F., and Day, S. (2002). Insar observations of the 1995 fogo, Cape Verde, eruption: implications for the effects of collapse events upon island volcanoes. *Geophys. Res. letters* 29, 47-1–47-4. doi:10.1029/2001gl013760

Arndt, N., Coltice, N., Helmstaedt, H., and Gregoire, M. (2009). Origin of archean subcontinental lithospheric mantle: some petrological constraints. *Lithos* 109, 61–71. doi:10.1016/j.lithos.2008.10.019

Barker, A. K., Hansteen, T. H., and Nilsson, D. (2019). Unravelling the crustal architecture of Cape Verde from the seamount xenolith record. *Minerals* 9, 90. doi:10.3390/min9020090

Barker, A. K., Troll, V. R., Carracedo, J. C., and Nicholls, P. A. (2015). The magma plumbing system for the 1971 teneguía eruption on la palma, canary islands. *Contributions Mineralogy Petrology* 170, 54–21. doi:10.1007/s00410-015-1207-7

Barker, A. K., Troll, V. R., Ellam, R., Hansteen, T. H., Harris, C., Stillman, C., et al. (2012). Magmatic evolution of the cadamosto seamount, Cape Verde: beyond the spatial extent of em1. *Contributions Mineralogy Petrology* 163, 949–965. doi:10.1007/s00410-011-0708-2

Beloša, L., Callegaro, S., Meyzen, C. M., Gaina, C., Polteau, S., Bizimis, M., et al. (2024). Deep mantle component and continental crust remobilization in the source of vesteris seamount, east Greenland margin. *Geochem. Geophys. Geosystems* 25, e2023GC011196. doi:10.1029/2023gc011196

Berthod, C., Médard, E., Di Muro, A., Hassen Ali, T., Gurioli, L., Chauvel, C., et al. (2021). Mantle xenolith-bearing phonolites and basanites feed the active volcanic ridge of Mayotte (Comoros archipelago, sw indian ocean). *Contributions Mineralogy Petrology* 176, 75–24. doi:10.1007/s00410-021-01833-1

Celli, N. L., Lebedev, S., Schaeffer, A. J., and Gaina, C. (2021). The tilted Iceland plume and its effect on the north atlantic evolution and magmatism. *Earth Planet. Sci. Lett.* 569, 117048. doi:10.1016/j.epsl.2021.117048

Damasceno, D., Scoates, J. S., Weis, D., Frey, F. A., and Giret, A. (2002). Mineral chemistry of mildly alkalic basalts from the 25 ma mont crozier section, kerguelen archipelago: constraints on phenocryst crystallization environments. *J. Petrology* 43, 1389–1413. doi:10.1093/petrology/43.7.1389

Danyushevsky, L. V. (2001). The effect of small amounts of h2o on crystallisation of mid-ocean ridge and backarc basin magmas. *J. Volcanol. Geotherm. Res.* 110, 265–280. doi:10.1016/s0377-0273(01)00213-x

Davidson, J., Morgan, D., Charlier, B., Harlou, R., and Hora, J. (2007). Microsampling and isotopic analysis of igneous rocks: implications for the study of magmatic systems. *Annu. Rev. Earth Planet. Sci.* 35, 273–311. doi:10.1146/annurev.earth.35.031306.140211

Dayton, K., Gazel, E., Wieser, P., Troll, V. R., Carracedo, J. C., La Madrid, H., et al. (2023). Deep magma storage during the 2021 la palma eruption. *Sci. Adv.* 9, eade7641. doi:10.1126/sciadv.ade7641

Deer, W. A. (1978). *Rock forming minerals. 2a. Single chain solicates*. 668.

Dobosi, G., and Fodor, R. (1992). Magma fractionation, replenishment, and mixing as inferred from green-core clinopyroxenes in pliocene basanite, southern Slovakia. *Lithos* 28, 133–150. doi:10.1016/0024-4937(92)90028-w

Dofal, A., Michon, L., Fontaine, F. R., Rindraharisaona, E., Barruol, G., and Tkalčić, H. (2022). Imaging the lithospheric structure and plumbing system below the Mayotte volcanic zone. *Comptes Rendus. Géoscience* 354, 47–64. doi:10.5802/crgeos.190

Dragone, G. N., and de Souza Bologna, M. (2024). Magmatic underplating, plumbing system, and carbon-enhanced electrical conductivity in the paraná magmatic province. *Phys. Earth Planet. Interiors* 351, 107185. doi:10.1016/j.pepi.2024.107185

Eisele, S., Freundt, A., Kutterolf, S., Hansteen, T. H., Klügel, A., and Irion, I. (2016). Evolution of magma chambers generating the phonolitic cão grande formation on santo antão, Cape Verde archipelago. *J. Volcanol. Geotherm. Res.* 327, 436–448. doi:10.1016/j.jvolgeores.2016.09.016

Fan, C., Xia, S., Zhao, F., Sun, J., Cao, J., Xu, H., et al. (2017). New insights into the magmatism in the northern margin of the s outh c hina s ea: spatial features and volume of intraplate seamounts. *Geochem. Geophys. Geosystems* 18, 2216–2239. doi:10.1002/2016gc006792

Feig, S. T., Koepke, J., and Snow, J. E. (2006). Effect of water on tholeiitic basalt phase equilibria: an experimental study under oxidizing conditions. *Contributions Mineralogy Petrology* 152, 611–638. doi:10.1007/s00410-006-0123-2

Gaina, C., Blischke, A., Geissler, W. H., Kimbell, G. S., and Erlendsson, Ö. (2017). Seamounts and oceanic igneous features in the ne atlantic: a link between plate motions and mantle dynamics. *Geol. Soc. Lond. Spec. Publ.* 447, 419–442. doi:10.1144/sp447.6

Gaina, C., Gernigon, L., and Ball, P. (2009). Palaeocene–recent plate boundaries in the ne atlantic and the formation of the jan mayen microcontinent. *J. Geol. Soc.* 166, 601–616. doi:10.1144/0016-76492008-112

GEBCO (2021). Gebco bathymetric compilation group 2021. *gebco 2021 grid - a continuous terrain model Glob. oceans land. nerc eds Br. Oceanogr. data centre noc* 1. doi:10.5285/C6612CBE-50B3-0CFF-E053-6C86ABC09F8F

Gernigon, L., Olesen, O., Ebbing, J., Wienecke, S., Gaina, C., Mogaard, J. O., et al. (2009). Geophysical insights and early spreading history in the vicinity of the jan mayen fracture zone, Norwegian–greenland sea. *Tectonophysics* 468, 185–205. doi:10.1016/j.tecto.2008.04.025

Gómez Dacal, M. L., Scheck-Wenderoth, M., Faleide, J. I., Abdelmalak, M. M., Bott, J., and Anikiev, D. (2023). Tracing the Iceland plume and north east atlantic breakup in the lithosphere. *Commun. Earth and Environ.* 4, 457. doi:10.1038/s43247-023-01120-w

González-García, D., Petrelli, M., Perugini, D., Giordano, D., Vasseur, J., Paredes-Mariño, J., et al. (2022). Pre-eruptive conditions and dynamics recorded in banded pumices from the el abrigo caldera-forming eruption (tenerife, canary islands). *J. Petrology* 63, egac009. doi:10.1093/petrology/egac009

Grønlie, G., and Talwani, M. (1978). Geophysical atlas: Norwegian-Greenland sea, vema res. ser. *lamont-doherty Geol. Obs. N. Y.* 4.

Haase, C., Ebbing, J., and Funck, T. (2017). *A 3d regional crustal model of the ne atlantic based on seismic and gravity data*. London: Geological Society. 447, 233–247. doi:10.1144/sp447.8

Haase, K. M., and Devey, C. W. (1994). The petrology and geochemistry of vesteris seamount, Greenland basin—an intraplate alkaline volcano of non-plume origin. *J. Petrology* 35, 295–328. doi:10.1093/petrology/35.2.295

Hempel, P., Schreiber, R., Johnson, L., and Thiede, J. (1991). The vesterisbanken seamount (Greenland basin): patterns of morphology and sediment distribution. *Mar. Geol.* 96, 175–185. doi:10.1016/0025-3227(91)90215-p

Herzberg, C. (2011). Identification of source lithology in the Hawaiian and canary islands: implications for origins. *J. Petrology* 52, 113–146. doi:10.1093/petrology/egq075

Iyer, S., Mehta, C., Das, P., and Kalangutkar, N. (2012). Seamounts: characteristics, formation, mineral deposits and biodiversity. *Geol. Acta* 10, 0295–0308. doi:10.1344/105.000001758

Jankovics, M. É., Dobosi, G., Embey-Isztin, A., Kiss, B., Sági, T., Harangi, S., et al. (2013). Origin and ascent history of unusually crystal-rich alkaline basaltic magmas from the western pannonian basin. *Bull. Volcanol.* 75, 1–23. doi:10.1007/s00445-013-0749-7

Jarosewich, E., and Boatner, L. (1991). Rare-earth element reference samples for electron microprobe analysis. *Geostand. Newsl.* 15, 397–399. doi:10.1111/j.1751-908x.1991.tb00115.x

Kamacı, Ö., and Altunkaynak, Ş. (2019). Magma chamber processes and dynamics beneath northwestern anatolia: insights from mineral chemistry and crystal size distributions (csds) of the kepsut volcanic complex (nw Turkey). *J. Asian Earth Sci.* 181, 103889. doi:10.1016/j.jseaes.2019.103889

Klügel, A., Hansteen, T. H., and Galipp, K. (2005). Magma storage and underplating beneath cumbre vieja volcano, la palma (canary islands). *Earth Planet. Sci. Lett.* 236, 211–226. doi:10.1016/j.epsl.2005.04.006

Klügel, A., Hoernle, K. A., Schmincke, H.-U., and White, J. D. (2000). The chemically zoned 1949 eruption on la palma (canary islands): Petrologic evolution and magma supply dynamics of a rift zone eruption. *J. Geophys. Res. Solid Earth* 105, 5997–6016. doi:10.1029/1999jb900334

Klügel, A., Longpré, M.-A., García-Cañada, L., and Stix, J. (2015). Deep intrusions, lateral magma transport and related uplift at ocean island volcanoes. *Earth Planet. Sci. Lett.* 431, 140–149. doi:10.1016/j.epsl.2015.09.031

Le Maitre, R., Bateman, P., Dudek, A., Keller, J., Lameyre, J., Le Bas, M., et al. (1989). *A classification of igneous rocks and glossary of terms. recommendations of the iugs subcommission on the systematics of igneous rocks*.

Leake, B. (1997). And 20 co-authors (1997). nomenclature of amphiboles: report of the subcommittee on amphiboles of the international mineralogical association commission on new minerals and mineral names. *Mineral. Mag.* 61, 295–321.

LeMaitre, R. W. (ed.) (2002). *Igneous rocks: a classification and glossary of terms: recommendation of the international union of geological sciences, subcommission on the systematics of igneous rocks* (Cambridge: Cambridge Univ. Press), 2.

Lessing, P., and Grout, C. M. (1971). Haünite from edwards, New York. *Am. Mineralogist J. Earth Planet. Mater.* 56, 1096–1100.

Liu, J.-Q., Chen, L.-H., Wang, X.-J., Zhang, H.-L., Zeng, G., Erdmann, S., et al. (2022). Olivine and melt inclusion chemical constraints on the nature and origin of the common mantle component beneath eastern asia. *Contributions Mineralogy Petrology* 177, 116. doi:10.1007/s00410-022-01981-y

Longpré, M.-A., Stix, J., Burkert, C., Hansteen, T., and Kutterolf, S. (2014). Sulfur budget and global climate impact of the ad 1835 eruption of cosigüina volcano, Nicaragua. *Geophys. Res. Lett.* 41, 6667–6675. doi:10.1002/2014gl061205

Longpré, M.-A., Troll, V. R., and Hansteen, T. H. (2008). Upper mantle magma storage and transport under a canarian shield-volcano, teno, tenerife (Spain). *J. Geophys. Res. Solid Earth* 113. doi:10.1029/2007jb005422

Ma, B., Liu, P.-P., Dick, H. J., Zhou, M.-F., Chen, Q., and Liu, C.-Z. (2024). Trans-lithospheric ascent processes of the deep-rooted magma plumbing system underneath the ultraslow-spreading sw indian ridge. *J. Geophys. Res. Solid Earth* 129, e2023JB027224. doi:10.1029/2023jb027224

MacDonald, A., Ubide, T., Mollo, S., Pontesilli, A., and Masotta, M. (2023). The influence of undercooling and sector zoning on clinopyroxene–melt equilibrium and thermobarometry. *J. Petrology* 64, egad074. doi:10.1093/petrology/egad074

Mertz, D. F., and Renne, P. R. (1995). Quaternary multi-stage alkaline volcanism at vesteris seamount (Norwegian—greenland sea): evidence from laser step heating 40ar/39ar experiments. *J. Geodyn.* 19, 79–95. doi:10.1016/0264-3707(94)e0001-b

Mertz, D. F., Sharp, W. D., and Haase, K. M. (2004). Volcanism on the eggvin bank (central Norwegian-Greenland sea, latitude ~71°N): age, source, and relationship to the Iceland and putative jan mayen plumes. *J. Geodyn.* 38, 57–84. doi:10.1016/j.jog.2004.03.003

Meyzen, C., Marzoli, A., Bellieni, G., and Levresse, G. (2016). Magmatic activity on a motionless plate: the case of east island, crozet archipelago (indian ocean). *J. Petrology* 57, 1409–1436. doi:10.1093/petrology/egw045

Michael, P. J., and Chase, R. L. (1987). The influence of primary magma composition, h 2 o and pressure on mid-ocean ridge basalt differentiation. *Contributions Mineralogy Petrology* 96, 245–263. doi:10.1007/bf00375237

Mollo, S., and Masotta, M. (2014). Optimizing pre-eruptive temperature estimates in thermally and chemically zoned magma chambers. *Chem. Geol.* 368, 97–103. doi:10.1016/j.chemgeo.2014.01.007

Mollo, S., Putirka, K., Misiti, V., Soligo, M., and Scarlato, P. (2013). A new test for equilibrium based on clinopyroxene–melt pairs: clues on the solidification temperatures of etnean alkaline melts at post-eruptive conditions. *Chem. Geol.* 352, 92–100. doi:10.1016/j.chemgeo.2013.05.026

Moreno, K. A., Thal, J., Bach, W., Beier, C., and Haase, K. M. (2021). Volcanic structures and magmatic evolution of the vesteris seamount, Greenland basin. *Front. Earth Sci.* 9, 711910. doi:10.3389/feart.2021.711910

Morimoto, N. (1988). Nomenclature of pyroxenes. *Mineralogy Petrology* 39, 55–76. doi:10.1007/BF01226262

Müller, R. D., Seton, M., Zahirovic, S., Williams, S. E., Matthews, K. J., Wright, N. M., et al. (2016). Ocean basin evolution and global-scale plate reorganization events since pangea breakup. *Annu. Rev. Earth Planet. Sci.* 44, 107–138. doi:10.1146/annurev-earth-060115-012211

Nikogosian, I., Bracco Gartner, A., Van Bergen, M., Mason, P., and Van Hinsbergen, D. J. (2018). Mantle sources of recent anatolian intraplate magmatism: a regional plume or local tectonic origin? *Tectonics* 37, 4535–4566. doi:10.1029/2018tc005219

O'Connor, J., Stoffers, P., Wijbrans, J., Shannon, P., and Morrissey, T. (2000). Evidence from episodic seamount volcanism for pulsing of the Iceland plume in the past 70 myr. *Nature* 408, 954–958. doi:10.1038/35050066

Pilet, S., Hernandez, J., and Villemant, B. (2002). Evidence for high silicic melt circulation and metasomatic events in the mantle beneath alkaline provinces: the na–fe-augitic green-core pyroxenes in the tertiary alkali basalts of the cantal massif (French massif central). *Mineralogy Petrology* 76, 39–62. doi:10.1007/s007100200031

Pouchou, J.-L., and Pichoir, F. (1991). "Quantitative analysis of homogeneous or stratified microvolumes applying the model "PAP"" in *Electron probe quantitation*. Editors K. F. J. Heinrich, and D. E. Newbury (Boston, MA: Springer US), 31–75. doi:10.1007/978-1-4899-2617-3_4

Putirka, K., Johnson, M., Kinzler, R., Longhi, J., and Walker, D. (1996). Thermobarometry of mafic igneous rocks based on clinopyroxene-liquid equilibria, 0–30 kbar. *Contributions Mineralogy Petrology* 123, 92–108. doi:10.1007/s004100050145

Putirka, K. D. (2008). Thermometers and barometers for volcanic systems. *Rev. mineralogy Geochem.* 69, 61–120. doi:10.2138/rmg.2008.69.3

Putirka, K. D., Mikaelian, H., Ryerson, F., and Shaw, H. (2003). New clinopyroxene-liquid thermobarometers for mafic, evolved, and volatile-bearing lava compositions, with applications to lavas from tibet and the snake river plain, Idaho. *Am. Mineralogist* 88, 1542–1554. doi:10.2138/am-2003-1017

Rickers, F., Fichtner, A., and Trampert, J. (2013). The Iceland–jan mayen plume system and its impact on mantle dynamics in the north atlantic region: evidence from full-waveform inversion. *Earth Planet. Sci. Lett.* 367, 39–51. doi:10.1016/j.epsl.2013.02.022

Schwarz, S., Klügel, A., and Wohlgemuth-Ueberwasser, C. (2004). Melt extraction pathways and stagnation depths beneath the madeira and desertas rift zones (ne atlantic) inferred from barometric studies. *Contributions Mineralogy Petrology* 147, 228–240. doi:10.1007/s00410-004-0556-4

Shore, M., and Fowler, A. D. (1996). Oscillatory zoning in minerals; a common phenomenon. *Can. Mineralogist* 34, 1111–1126.

Sobolev, A. V., Hofmann, A. W., Sobolev, S. V., and Nikogosian, I. K. (2005). An olivine-free mantle source of Hawaiian shield basalts. *Nature* 434, 590–597. doi:10.1038/nature03411

Soltanmohammadi, A., Grégoire, M., Ceuleneer, G., Benoit, M., Bédard, L. P., Gouy, S., et al. (2021). Origin of antecrysts in igneous rocks from the salavat range (nw Iran): an explanation for the geochemical signature of potassic alkaline rocks. *J. Petrology* 62, egab031. doi:10.1093/petrology/egab031

Staudingel, H., and Clague, D. A. (2010). The geological history of deep-sea volcanoes: biosphere, hydrosphere, and lithosphere interactions. *Oceanography* 23, 58–71. doi:10.5670/oceanog.2010.62

Steinberger, B., and Becker, T. W. (2018). A comparison of lithospheric thickness models. *Tectonophysics* 746, 325–338. doi:10.1016/j.tecto.2016.08.001

Stormer, J. C., Pierson, M. L., and Tacker, R. C. (1993). Variation of F and Cl X-ray intensity due to anisotropic diffusion in apatite during electron microprobe analysis. *Am. Mineralogist* 78, 641–648.

Straub, S. M., LaGatta, A. B., Martin-Del Pozzo, A. L., and Langmuir, C. H. (2008). Evidence from high-ni olivines for a hybridized peridotite/pyroxenite source for orogenic andesites from the central mexican volcanic belt. *Geochem. Geophys. Geosystems* 9. doi:10.1029/2007gc001583

Streck, M. J. (2008). Mineral textures and zoning as evidence for open system processes. *Rev. Mineralogy Geochem.* 69, 595–622. doi:10.2138/rmg.2008.69.15

Svetov, S. A., Chazhengina, S. Y., and Stepanova, A. V. (2020). Geochemistry and texture of clinopyroxene phenocrysts from paleoproterozoic picrobasalts, Karelian craton, fennoscandian shield: records of magma mixing processes. *Minerals* 10, 434. doi:10.3390/min10050434

Tapu, A., Ubide, T., and Vasconcelos, P. (2023). Increasing complexity in magmatic architecture of volcanoes along a waning hotspot. *Nat. Geosci.* 16, 371–379. doi:10.1038/s41561-023-01156-9

Tapu, A. T., Ubide, T., and Vasconcelos, P. M. (2022). Plumbing system architecture of late-stage hotspot volcanoes in eastern Australia. *J. Petrology* 63, egac015. doi:10.1093/petrology/egac015

Ubide, T., and Kamber, B. S. (2018). Volcanic crystals as time capsules of eruption history. *Nat. Commun.* 9, 326. doi:10.1038/s41467-017-02274-w

Ubide, T., Larrea, P., Becerril, L., and Galé, C. (2022). Volcanic plumbing filters on ocean-island basalt geochemistry. *Geology* 50, 26–31. doi:10.1130/g49224.1

Ubide, T., Márquez, Á., Ancochea, E., Huertas, M. J., Herrera, R., Coello-Bravo, J. J., et al. (2023). Discrete magma injections drive the 2021 la palma eruption. *Sci. Adv.* 9, eadg4813. doi:10.1126/sciadv.adg4813

Ubide, T., McKenna, C. A., Chew, D. M., and Kamber, B. S. (2015). High-resolution la-icp-ms trace element mapping of igneous minerals: in search of magma histories. *Chem. Geol.* 409, 157–168. doi:10.1016/j.chemgeo.2015.05.020

Ubide, T., Mollo, S., Zhao, J.-x., Nazzari, M., and Scarlato, P. (2019). Sector-zoned clinopyroxene as a recorder of magma history, eruption triggers, and ascent rates. *Geochimica Cosmochimica Acta* 251, 265–283. doi:10.1016/j.gca.2019.02.021

Villaseca, C., García Serrano, J., and Orejana, D. (2020). Pyroxenites and megacrysts from alkaline melts of the calatrava volcanic field (central Spain): inferences from trace element geochemistry and sr-nd isotope composition. *Front. Earth Sci.* 8, 132. doi:10.3389/feart.2020.00132

Voss, M., Schmidt-Aursch, M. C., and Jokat, W. (2009). Variations in magmatic processes along the east Greenland volcanic margin. *Geophys. J. Int.* 177, 755–782. doi:10.1111/j.1365-246x.2009.04077.x

Wieser, P. E., Kent, A. J., Till, C. B., Donovan, J., Neave, D. A., Blatter, D. L., et al. (2023). Barometers behaving badly i: assessing the influence of analytical and experimental uncertainty on clinopyroxene thermobarometry calculations at crustal conditions. *J. Petrology* 64, egac126. doi:10.1093/petrology/egac126

Yang, W., Zhao, B., Yu, H., Xu, J., Wei, F., and Cui, X. (2023). Mineralogical constraints on magma recharge and mixing of the post-collisional potassic volcanic rocks in dahongliutan, nw Tibetan plateau. *Minerals* 13, 1463. doi:10.3390/min13121463

Zanon, V. (2015). Conditions for mafic magma storage beneath fissure zones at oceanic islands. The case of São Miguel Island (Azores archipelago). *Geol. Soc. Lond. Spec. Publ.* 422, 85–104. doi:10.1144/SP422.4

Zhang, T., Lin, J., and Gao, J. (2020). Asymmetric crustal structure of the ultraslow-spreading mohns ridge. *Int. Geol. Rev.* 62, 568–584. doi:10.1080/00206814.2019.1627586

Ziem à Bidias, L. A., Chauhan, H., Mekala, R. M., and Rao, N. C. (2021). Green core clinopyroxenes from basanites of petpenoun volcanoes, noun plain, Cameroon volcanic line: chemistry and genesis. *Bull. Volcanol.* 83, 13–20. doi:10.1007/s00445-021-01437-4